Manipulating Nonproportionality of Strontium Iodide Crystals with High-Flux Irradiation by ^{137}Cs Gamma Rays

By

David D. Caudel

Dissertation

Submitted to the Faculty of the

Graduate School of Vanderbilt University

in partial fulfillment of the requirements

for the degree of

DOCTOR OF PHILOSOPHY

in

Physics

May 2017

Nashville, Tennessee

Approved: Keivan Stassun, Ph.D.

Arnold Burger, Ph.D.

Richard Haglund, Ph.D.

Ashley Stowe, Ph.D.

In dedication to my children and in loving memory of my father.

Also, to the Fisk-to-Vanderbilt Bridge Program, for giving me the chance to fulfill my dream of becoming a physicist.

ACKNOWLEDGMENTS

The work in this dissertation has been supported by the following entities and funding sources: the Fisk-to-Vanderbilt Bridge Program, the BOLD fellowship, the GAANN fellowship CFDA 84.200, the NSF Grant HRD 1547757 (CREST-BioSS Center), the Vanderbilt Discovery Grant, and Fisk University's subaward with ORNL GO under prime contract DE-AC52-07NA27344 from the United States Department of Energy.

TABLE OF CONTENTS

LIST OF TABLES

LIST OF FIGURES

CHAPTER 1

INTRODUCTION

1.1 Overview

The objective of this work is to examine scintillators for astrophysics applications – gamma-ray spectrometers used in satellites to study the cosmos. Some cosmic objects, such as pulsars, quasars, and black holes, are only detectable in the gamma/x-ray regimes. To study such phenomena, NASA builds space-based telescopes outfitted with scintillators, and successive generations of these devices have led to new discoveries, such as the discovery of hundreds of new gamma and x-ray sources such as quasars, black holes and pulsars (Reddy et al., 2016).

The Fermi Gamma-ray Space Telescope (FGST) was recently used to discover gamma-ray "bubbles" extending above and below our galaxy's center, as illustrated in **Figure 1.1**. Each lobe extends more than 25,000 light years from the galactic plane and is estimated to be less than a few million years old (Su et al., 2010). The FGST has fourteen

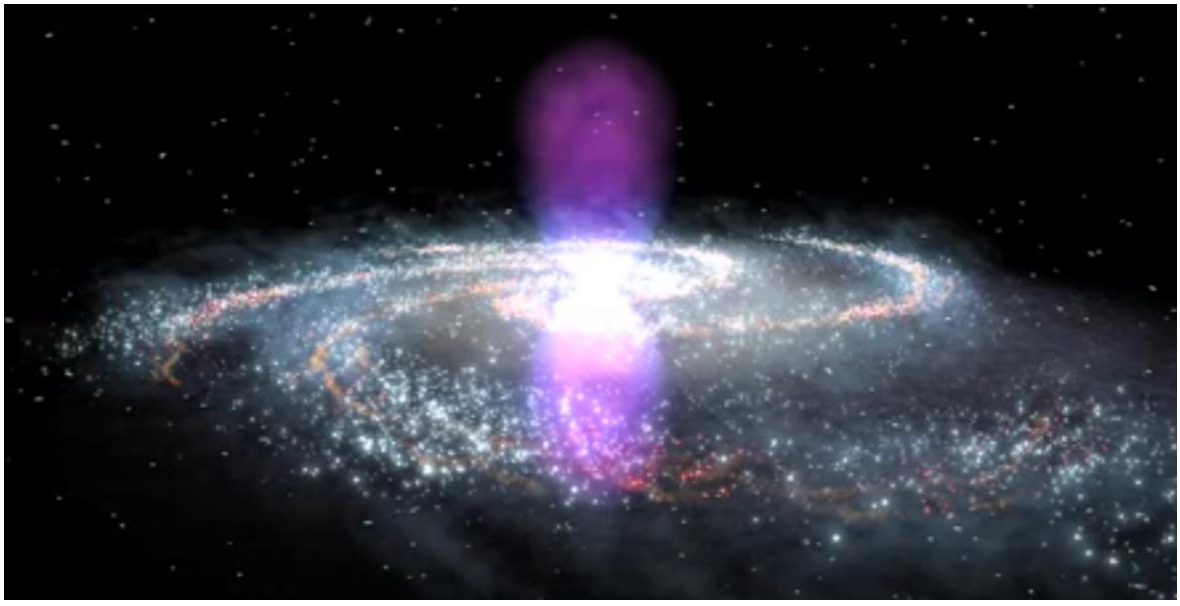

Figure 1.1: Animation of gamma-ray lobes extending 25,000 light years from the center of the Milky Way galaxy. (NASA, 2010a)

scintillators used to study gamma-ray bursts: twelve sodium iodide (NaI) crystals, sensitive up to 1 MeV and used to determine burst locations, and two bismuth germinate ($Bi_4Ge_3O_{12}$, known as BGO) crystals, for energies above 200 keV (Guiriec et al., 2010).

SCINTILLATION PROPERTIES OF ALKALINE EARTH HALIDE CRYSTALS[1]

Scintillator	ρ (g/cm^3)	Z_{eff} [a]	Emission Peak (nm)	Estimated Band Gap, E_g [b] (eV)	Theoretical Maximum LY [d] (Ph/MeV)	Measured β LY (Ph/MeV)	Measured γ LY (Ph/MeV)	Measured Resolution (662 keV)
SrI_2 undoped	4.549	49.4	560	3.7 [c]	111,000	62,000	38,000	6.7%
SrI_2 (Eu, 6%)	4.549	49.4	435	3.7 [c]	111,000	110,000	115,000	2.8%
$SrBr_2$(Eu, 0.5%)	4.216	36.1	410	4.0	100,000	25,000	20,000	7%
BaI_2(Eu, 0.5%)	5.150	54.1	422	3.9	103,000	40,000	35,000	8%
$BaBr_2$(Eu, 0.1%)	4.781	45.5	406	4.1	98,000	22,000	16,000 [e]	11% [e]
CaI_2(Eu, 0.5%)	4.000	48.0	467	3.5	114,000	110,000	110,000	5.2% [f]
$LaBr_3$(Ce)	5.080	44.1	360	4.5	89,000	60,000	60,000	2.6%

Table 1.1: Scintillation properties of alkaline earth halide crystals (Cherepy et al., 2009b).

One scintillator in particular is the focus of this work: strontium iodide doped with europium ($SrI_2:Eu^{2+}$). As sources in the cosmos may be thousands or millions or even billions of light years away, the flux of incoming radiation are typically much smaller than that of terrestrial sources. Gamma ray spectrometers used to detect weak sources need detector materials with superior energy resolution, to resolve signal over noise, and the ability to be grown cheaply to large volumes, maximizing the capture of gamma rays. Strontium iodide shows great promise as one such material (Cherepy et al., 2009a; Cherepy et al., 2009b; Cherepy et al., 2008). Another issue is how well the scintillator material holds up to cosmic radiation damage. Commercial and hardened CMOS devices intended for space-based applications are typically tested with high-flux gamma irradiation, often from a ^{60}Co source, to determine how well such devices would function in space (Fleetwood et al., 1988). Although cosmic radiation differs from gamma radiation, comparisons of radiation effects in space, high-energy particle beams, and gamma sources show that high-flux gamma irradiation testing is a good predictor for space-based applications (Winokur et al., 1986).

1.2 Scintillator Physics

A scintillator is a crystal that absorbs incoming ionizing radiation, such as gamma rays and x-rays, and typically emits that energy in the form of visible light. The intensity of light (number of photons emitted) is, ideally, directly proportional to the energy of the ionizing event, assuming no loss through secondary effects. When coupled to an electronic light sensor such as a photomultiplier tube (PMT) or photodiode, the number of photons generated in each event may be counted. In this manner, a scintillator may be used to measure the energy of each ionizing particle. An ionizing particle interacts with the scintillator in one of three significant ways: photoelectric absorption, Compton scattering, and pair production. With Compton scattering, the ionizing particle collides with an electron, imparting a fraction of its energy into the scintillation material. As only part of the energy is deposited while the ionizing particle escapes, the energy of the ionizing particle remains unknown and so Compton scattering events are typically discounted. For low-energy gamma rays (up to several hundred keV), pair production plays a minimal role, as the minimum energy needed in pair production is 1.02 MeV. Pair production becomes dominant at 5-10 MeV (Knoll, 2010).

Photoelectric absorption is the dominant mechanism for measuring the energy of ionizing particles absorbed by the scintillator for low-energy gamma rays. It produces a photoelectron, or hot electron, with kinetic energy equal to the energy of the ionizing particle minus the binding energy of the hot electron. As the hot electron leaves a hole in its original shell (typically the *K* shell), an outer-shell electron either drops to fill this hole, emitting an x-ray in the process, or an Auger electron is produced. X-rays typically travel a millimeter or less (Auger electrons far less than that) before being reabsorbed. As the hot electron travels through the material, it loses kinetic energy through collisions with other

electrons, freeing these electrons, producing electron-hole pairs in its path. If the x-ray or Auger electron is also absorbed, this also produces electron-hole pairs. Ideally, these electron-hole pairs form excitons and migrate to activator sites, where they are captured and recombined to emit light at a specific wavelength, typically visible light (Knoll, 2010).

In Vasil'ev et al., 2014, Monte-Carlo simulations of the hot electron track illustrate the spacing of electrons and holes generated as the hot electron travels through the material, illustrated in **Figure 1.2**. At the start of the track, where the hot electron has the most kinetic energy, electrons freed and their corresponding holes are spaced further apart, as greater kinetic energy is imparted by the hot electron. Near the end of the track, where the hot electron has lost most of its kinetic energy, not only are electrons and holes bunched closer together, but each pair is created closer to the next, as little kinetic energy is imparted by the hot electron and electron-hole pairs are created closer to one another.

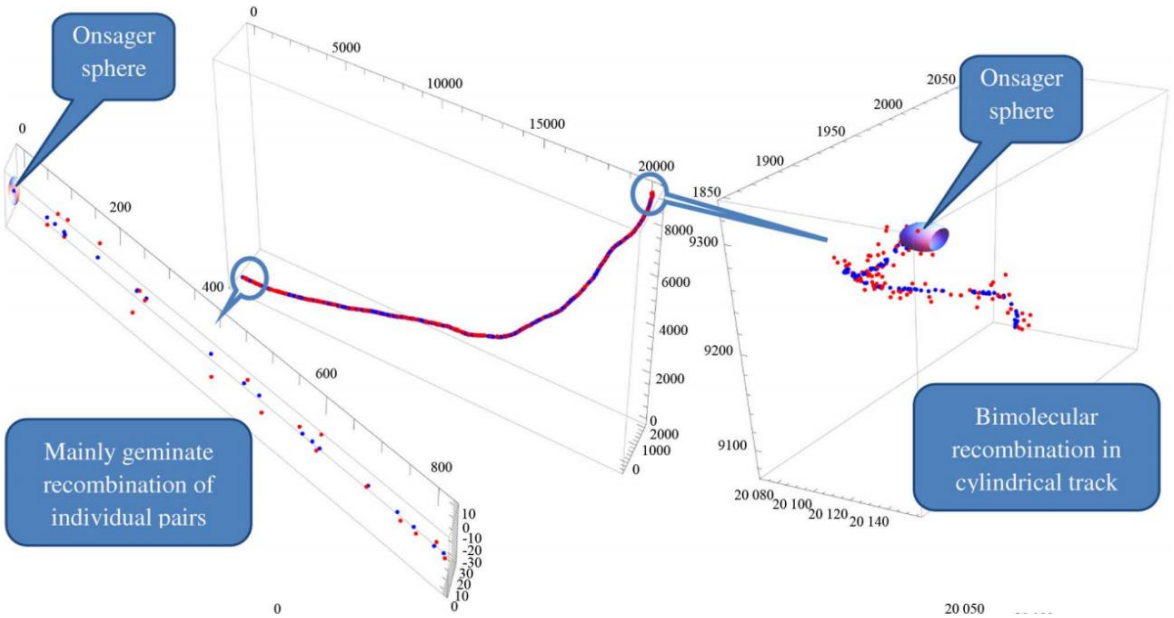

Figure 1.2: Monte-Carlo simulation of track structure for 30 keV electrons at thermalization length of 6 nm for electrons (shown as red dots) and 0.6 nm for holes (shown as blue dots). All axis labels are in nm. Onsager sphere refers to the radius where the thermal energy matches the Coulombic attraction between the electron and hole, detailed further in 1.4. (Vasil'ev et al., 2014)

1.3 Energy Resolution

Measuring a monoenergetic source of radiation should, ideally (assuming an infinitely short lifetime for the emitter), produce a mathematical delta function in the energy spectrum at that energy, but fluctuations between events due to signal losses typically leads to a Gaussian distribution of the signal. Energy resolution, used to quantify this spread, is calculated by taking the full width at half maximum of the Gaussian, divided by the actual energy (typically at the centroid of the peak) and expressing as a percentage (Knoll, 2010).

Detectors with narrow energy resolutions are considered superior to those with wide energy resolutions. Multiple radiation sources may have energy values close to one another, only distinguishable among detectors with superior (narrow) energy resolution. Energy resolution also affects signal-to-noise, how high the peak rises over the background signal, as narrower energy resolutions result in taller Gaussian peaks. **Figure 1.3** compares the gamma spectrum of ^{239}Pu for a series of gamma spectrometers made of various crystals, with energy resolution getting wider from the bottom spectrum to the top. High-purity germanium has the best energy resolution, often much less than 1%, so each peak approaches a delta function and is clearly distinguishable from one another. Sodium iodide on top has the widest energy resolution, and the fine detail of the spectrum is lost to a few broad peaks. Note that the vertical scale is logarithmic and vertically offset to distinguish each spectrum – the narrower the energy resolution, the higher the peak, as all the counts for each peak raise the signal over background.

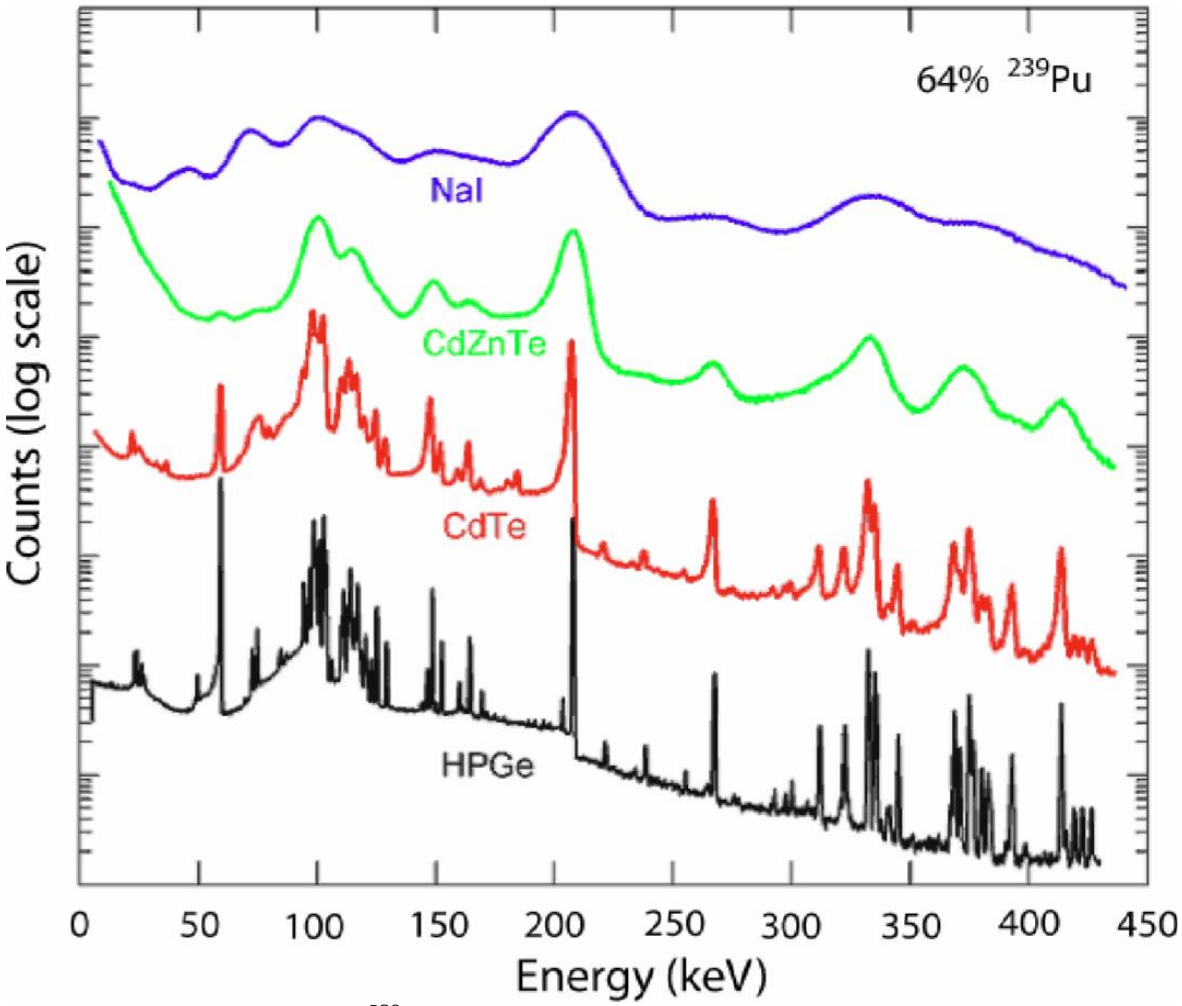

Figure 1.3: Spectra of 64% ^{239}Pu source comparing sodium iodide (NaI), a scintillator, and three semiconductors: cadmium zinc telluride (CdZnTe), cadmium telluride (CdTe), and high-purity germanium (HPGe). (Medalia, 2010)

While energy resolution is experimentally calculated as a peak's full width at half maximum (FWHM) divided by the centroid of the peak, it is physically described as the squared sum of three contributions:

$$R^2 = R_{PMT}^2 + R_{inh}^2 + R_{nPR}^2$$

where R_{PMT} is the contribution from the photodetector (the transfer of scintillation photons from the crystal to the PMT, gain and Poisson statistics); R_{inh} is the contribution from crystal inhomogeneities; and R_{nPR} is the contribution from the nonproportional response – described in detail below (Dorenbos et al., 1995). For the R_{PMT} term, contribution to

energy resolution is proportional to $N^{-1/2}$, where N is the mean number of photons captured by the PMT from the scintillation event (Dorenbos et al., 1995). For the R_{inh} term, purification of starting materials and growth conditions can minimize its contribution to energy resolution. For the R_{nPR} term, variations in the loss of signal, as a function of energy, leads to a broadening of energy resolution. For strontium iodide, this broadening due to nonproportionality is calculated to be the dominant effect limiting energy resolution, at or more than doubling the width (Cherepy et al., 2009b).

1.4 Nonproportionality

Research since the 1940s focused on improving the R_{PMT} and R_{inh} terms, however in recent years attention has shifted to the least-understood term: R_{nPR}. Study of nonproportionality and its effects on energy resolution is an active area of research (Payne et al., 2009; Payne et al., 2011; Payne et al., 2014; Beck et al., 2015). One method found to alter nonproportionality is the use of codopants, which demonstrated that improving proportionality also improves energy resolution (Alekhin et al., 2013a; Alekhin et al., 2013b; Yang et al., 2015). The present work also introduces a new method of altering nonproportionality through high-flux gamma irradiation.

Although nonproportionality is not fully understood, some predictive models fit well to data. By measuring the nonproportionality curves of several types of scintillators, Payne et al., 2009, developed a model that describes the carrier dynamics for the light yield versus electron energy. **Figure 1.4** shows how well this model fits to published data for several types of scintillators. They adapted the theory of Onsager (adopted from the work of Hoffman et al., 1991) to explain how carriers form excitons that arrive at activator sites to recombine and emit photons. They also employed the theory of Birks (Birks, 1964) to

allow for exciton-exciton annihilation.

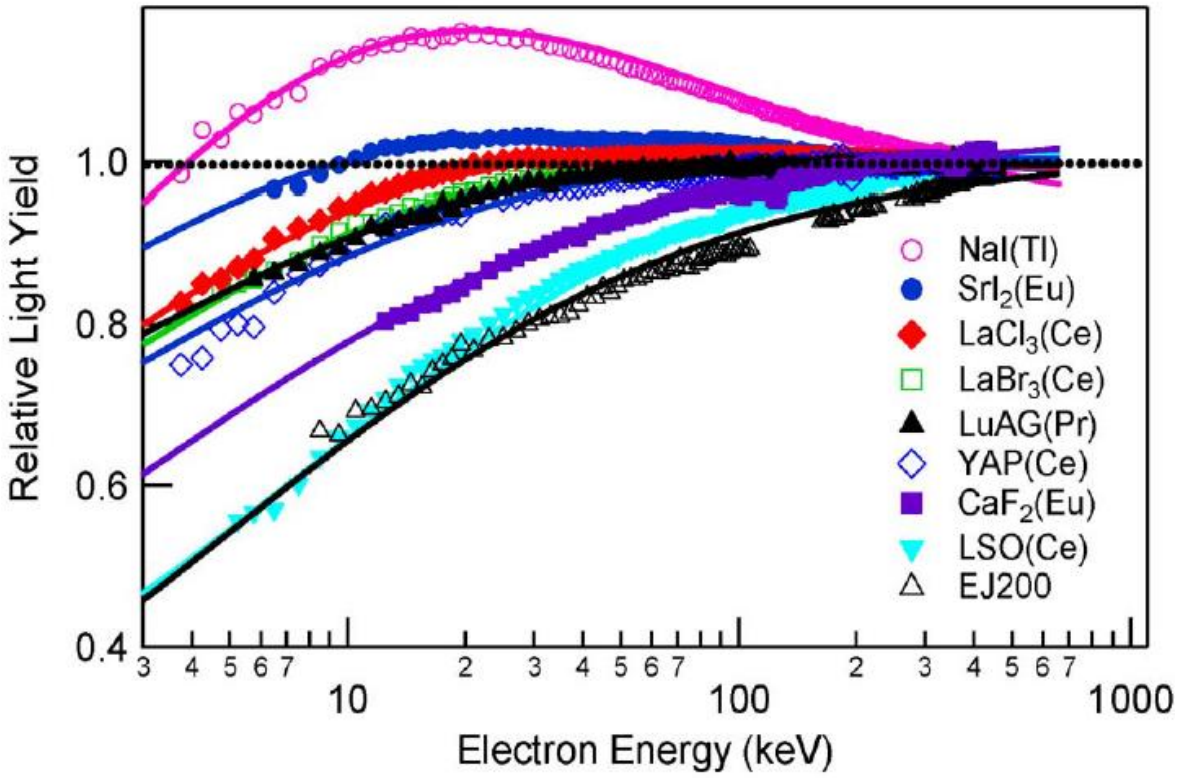

Figure 1.4: Nonproportionality curves of several types of scintillator, fitted to data obtained via the Scintillator Light Yield Nonproportionality Compton Instrument (SLYNCI). SLYNCI measures both the Compton scatter in the scintillator and recoiled gamma photon in one of several high-purity germanium detectors to determine the true energy of the Compton scatter in the scintillator. (Payne et al., 2011)

According to this model (Payne et al., 2009), the Onsager mechanism becomes dominant when the hot electron moves so quickly through the material that freed electrons drift too far from the corresponding holes and fail to form excitons. This mechanism is governed by the following equation:

$$\eta_{ONS} = 1 - \eta_{EXC} exp\left(\frac{-\frac{dE}{dx}}{\left(\frac{dE}{dx}\right)_{ONS}}\right)$$

where η_{ONS} is the electron-hole recombination efficiency and η_{EXC} is the number of excitons formed by electron-hole recombination. The Onsager radius, the point at which an

electron-hole pair Coulombic and thermal energies match, is given by:

$$\frac{e^2}{\varepsilon r_{ONS}} = kT$$

where ε is the static dielectric constant (3.86 for strontium iodide), e is the elemental electron charge and kT is the thermal energy. Beyond this distance, thermal energy in the electron-hole pair is greater than the Coulombic attraction, thus the electron and hole may drift apart, resulting in a loss of signal. For example, at room temperature (kT is 25.7 meV at 298 K) strontium iodide has an Onsager radius of approximately 14.5 nm – this is the critical distance at which thermal energy and Coulombic energy matches.

The Birks mechanism becomes dominant as the hot electron slows, where many excitons form in close proximity to one another – as the distance between excitons diminish, the likelihood that they combine with one another before making their way to an activator increase. This mechanism is governed by the following equation:

$$\eta_{BIRKS} = \left[1 + \left(\frac{\left(\frac{dE}{dx}\right)}{\left(\frac{dE}{dx}\right)_{BIRKS}}\right)\right]^{-1},$$

where η_{BIRKS} is the electron-hole loss, $\left(\frac{dE}{dx}\right)$ is the measure of exciton concentration, and $\left(\frac{dE}{dx}\right)_{BIRKS}$ is the fitting parameter related to the strength of the exciton-exciton annihilation mechanism (Payne et al., 2009).

Although there are likely other factors to nonproportionality, these two effects demonstrate how energy resolution degrades. At a given energy, a variable number of electron-hole pairs are lost, varying the signal and broadening the Gaussian distribution. Models have been developed for each process thought to affect scintillation with a host of variables, and many of the parameters these models depend on have yet to be accurately

measured. At present, it is unclear which of these parameters dominate nonproportionality, but a fully predictive model of scintillator proportionality seems plausible once enough of these parameters have been experimentally determined (Moses et al., 2012). This work seeks to expand towards that end by exploring a method of altering proportionality through radiation damage.

CHAPTER 2

RADIATION DAMAGE OF STRONTIUM IODIDE CRYSTALS DUE TO IRRADIATION BY ^{137}CS GAMMA RAYS: A NOVEL APPROACH TO ALTERING NONPROPORTIONALITY

Here we expand and adapt from work published in the Nuclear Instruments and Methods in Physics Research A, 2016, 835, 177-181.

2.1 Abstract

Strontium iodide doped with europium ($SrI_2:Eu^{2+}$) is a new scintillator being developed for use in high-energy astrophysical detectors with excellent energy resolution. Nonproportionality is the primary limiting factor to improving its energy resolution, although the physics of nonproportionality is not yet fully understood. In the past few years, co-dopants have been used to alter nonproportionality. By irradiating a $SrI_2:Eu^{2+}$ sample with a 2,255 Ci ^{137}Cs source, we explore both the crystal's potential for space-based applications in a radiation environment and this new method of altering nonproportionality. At ~6,200 Gy irradiation, a drop of 7.8% at 700 nm and a drop of 14.1% at 450 nm were seen in the transmission spectrum. Nonproportionality was also reduced after irradiation, shifting from 87% to 101% of the theoretical light yield at 32.1 keV, while the 4.7 keV peak decreased 40% closer to its theoretical value. We propose a novel method of altering the nonproportionality of scintillators, using radiation-induced F-centers in place of co-dopants.

2.2 Introduction

Active space-based gamma observation research includes the study of black holes, pulsars, and quasars, some of which cannot be detected except in the x-ray and gamma-ray regimes. Since the early 90s, NASA has been using space-based telescopes equipped with scintillators to study such phenomena, and successive generations of these devices rely on advances in technology to make new discoveries (Reddy 2016). Used as gamma spectrometers, scintillators are an important component in space observatories for high-energy events.

When testing the viability of commercial and hardened CMOS devices for space-based applications, ^{60}Co irradiation is typically used to simulate the radiation of space and estimate how well such devices would perform in that environment (Fleetwood et al., 1989). Similar defects are created via ^{137}Cs irradiation (Fleetwood et al., 1988). Previous studies show heavy scintillation crystals such as fluorides, tungstates, and BGO ($Bi_4Ge_3O_{12}$) crystals can recover from 10^5 Gy(^{60}Co) doses from a few days to a couple of weeks (Kozma et al., 2003). For halides such as CsI and BaF_2, recovery from radiation damage is slower, on the order to weeks or months at room temperature (Grupen et al., 2011). Prior to this study, to the best of our knowledge radiation damage and recovery of SrI_2 has never been published.

$SrI_2:Eu^{2+}$ is a scintillator that shows potential for the next generation of gamma spectrometers. Energy resolution at 662 keV has been demonstrated at 2.6% (Boatner et al., 2013). By comparison, cadmium zinc telluride (CZT), a semiconductor, has an energy resolution of 2% (Ramachers, 2007). $SrI_2:Eu^{2+}$ is less expensive to manufacture compared to CZT, and may be grown to much larger dimensions, leading to more efficient detectors (Cherepy et al., 2009a). CZT is superior to $SrI_2:Eu^{2+}$ only in terms of energy resolution, but

calculations indicate that this scintillator may one day match or even improve upon the energy resolution of CZT: the contribution due to nonproportionality is estimated at 1.4% (Cherepy et al., 2009b). This implies that, if nonproportionality were eliminated, the energy resolution would be less than 1.5%. Though eliminating nonproportionality is not feasible, reducing its impact would lead to superior energy resolution. If the resolution of SrI_2:Eu^{2+} were dropped below 2%, this would be a major breakthrough for gamma spectrometers, as it would combine the best features of both scintillators and semiconductors.

Energy resolution can be expressed by the equation $R^2 = R_{PMT}^2 + R_{inh}^2 + R_{nPR}^2$, where R_{PMT} is the contribution from the PMT (the transfer of scintillation photons from the crystal to the PMT, gain and Poisson statistics); R_{inh} is the contribution from crystal inhomogeneities; and R_{nPR} is the contribution from the nonproportional response (Dorenbos et al., 1995).

Although the first two terms of this equation have been extensively researched, the contribution from nonproportionality is currently an active area of research (Payne et al., 2009; Payne et al., 2011; Payne et al., 2014; Beck et al., 2015). For Eu-activated scintillators such as SrI_2:Eu, the contribution due to nonproportionality is the dominant factor limiting energy resolution (Dorenbos 2010).

One proposed method of varying the nonproportionality of scintillators is through the use of co-dopants. In *Alekhin et al., 2013a*, the addition of Ca, Sr, and Ba co-doping to $LaBr_3$:Ce (5%) improved proportionality, and with Sr co-doping they achieved a record low value for energy resolution of 2% at 662 keV. What limits the development of $LaBr_3$:Ce as a scintillator for space-based applications is its self-activity; pure $LaBr_3$ contains the ^{138}La radioactive isotope which may impact energy measurements below 1.5

MeV and limit the size of useful detectors (Keman, 2006). In *Yang et. al., 2015*, co-doping NaI:Tl with Sr and Ce exhibited better energy resolution and significantly improved proportionality. These works demonstrate that co-doping may be used to reduce nonproportionality and improve the energy resolution of scintillators.

The exact nature of how co-doping affects nonproportionality is not yet fully understood, although co-doping is suggested to either reduce the nonradiative recombination rate, increase the probability that electron-hole pairs escape from the quenching phase, or increase the trapping rate of activators (Alekhin et al., 2013b). In Beck et al., 2015, when calculating gamma nonproportionality from electron nonproportionality data, equations that account for traps lead to a better fit. This may indicate that traps from co-doping may play a role. Consider the bandgap, where an activator sits in the forbidden region: a co-dopant may also rest in this zone, perhaps as a "stepping stone" for excitons on their way to activator sites.

Co-doping may impart defects when compared to base crystals. For ceramics, co-dopants were shown to segregate to grain boundaries, where they aided in blocking such boundaries from propagating through the system (lattice hardening) (Li et al., 1999; Cho et al., 1999). Thus, a co-doped crystal may lose some of its co-dopant by impurity segregation and the lattice structure may be subtly different from a base crystal grown under the same conditions. Also, growing two crystals side by side with identical growth conditions may still lead to some variability. These issues may complicate comparisons between base and co-doped crystals when determining a co-dopant's impact on nonproportionality.

We introduce a novel method to introduce defects that may alter the nonproportionality of a crystal while avoiding the limitations of co-dopants: high-dose irradiation. In scintillators, radiation damage is predominantly expressed as the formation

of color centers (F-centers), where an ion in the lattice is displaced, leaving a vacancy where an electron can become trapped (Zhu, 1998). Such trapped electrons may be excited from their ground states, behaving like dopants. By thermal annealing at room temperature, displaced ions may eventually return to such vacancies, and many scintillators typically recover from radiation damage within days or weeks, though some scintillators take much longer (Zhu, 1998). The speed of this recovery depends on the depth of the induced traps, with slower recovery reflecting deeper traps (Zhu, 1998). By testing a sample, irradiating to form F-centers, then retesting, limitations due to varying growth conditions, lattice hardening and impurity segregation can be avoided. Thus, the impact of F-centers on nonproportionality may be assessed in an otherwise identical crystal.

In this study, radiation damage of $SrI_2:Eu^{2+}$ (2.5%) is assessed through transmission spectra and gamma spectra before and after irradiation. By these methods, radiation damage is quantified, recovery is assessed, and the impact on nonproportionality is explored.

2.3 Experimental Results

Samples were harvested from a $SrI_2:Eu^{2+}$ (2.5%) boule grown at Fisk University using the vertical Bridgman method and cut and polished to dimensions of approximately $1\times1\times1.4\ cm^3$. Samples were irradiated using a Shepherd Mark I Cesium-137 Irradiator Model 68, which was commissioned in September 1981 with a 5,000 Ci ^{137}Cs source. With a half-life of 30.17 years (Unterweger et al., 2010), the activity of the source was calculated to be 2,255 Ci during the experiment. The sample was hermetically sealed in quartz during both the irradiation and the measurement of the transmission spectra. The

crystal was sealed in an argon atmosphere rather than being immersed in light mineral oil, to avoid any possible interactions between oil/surface and irradiation.

The irradiator dose rate was calibrated with an ionization chamber in terms of Gy(tissue)/min using the appropriate mass energy-absorption coefficients for tissue $\left({}^{\mu_{en}}/_{\rho} = \mu_{tissue}\right)$ and was converted for SrI_2 $\left({}^{\mu_{en}}/_{\rho} = \mu_{SrI_2}\right)$. These were calculated using values found in the National Institute of Standards and Technology websource (Hubbell et al., 2004).

To calculate for SrI_2 we use the following equation;

$$\mu_{SrI_2} = \frac{(N_I \times M_I \times \mu_I) + (N_{Sr} \times M_{Sr} \times \mu_{Sr})}{(N_I \times M_I) + (N_{Sr} \times M_{Sr})} \qquad (2.1a)$$

where N is the relative ratio number of atoms, M is the molar mass for each element in the crystal and μ is the mass energy-absorption coefficient of the respective element.
So (at 600 keV):

$$\mu_{SrI_2} = \frac{(2 \times 126.9045 \times \mu_I) + (1 \times 87.62 \times \mu_{Sr})}{(2 \times 126.9045) + (1 \times 87.62)} \cong 0.0342\ {}^{cm^2}/_{g} \qquad (2.1b)$$

To calculate the dose rate,

$${Gy(SrI_2)}/_{min} = \left(\frac{\mu_{SrI_2}}{\mu_{tissue}}\right) \times {Gy(tissue)}/_{min} \times 2^{-\left(\frac{t}{t_{1/2}}\right)} \qquad (2.2a)$$

so (at 600 keV):

$${Gy(SrI_2)}/_{min} = \left(\frac{0.0342}{0.0324}\right) \times 25.29 \times 2^{-\left(\frac{4.137yrs}{30.17yrs}\right)} = 24.27 \qquad (2.2b)$$

The sample was irradiated for 256 minutes which produces a dose of approximately 6,200

Gy.

Optical transmission spectra were measured using a Varian Cary 500 Scan UV-Vis-NIR Spectrophotometer with an empty quartz holder used as a baseline. Quartz container was sealed with SGC BC600 Optical Cement in an argon-filled glovebox which had moisture level <1 ppm. This optical cement, a two-part epoxy, has been previously tested at Fisk University to ensure it does not interact with SrI_2 while curing in an argon atmosphere.

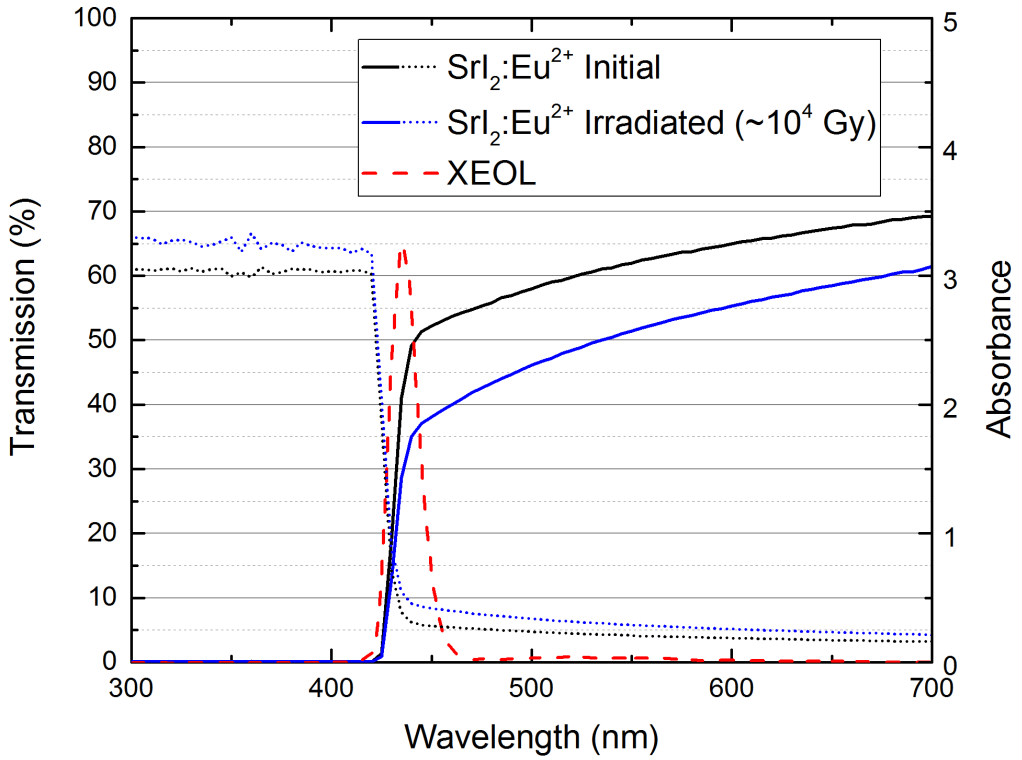

Figure 2.1: Comparison of optical transmission (solid lines) and absorbance (dotted lines) spectra before and after irradiation of $SrI_2:Eu^{2+}$. X-ray Excited Optical Luminescence (XEOL) of an undamaged $SrI_2:Eu^{2+}$ crystal added to illustrate absorption edge (in arbitrary units).

In order to quantify the reproducibility of the transmission spectra we repeated a scan over two days which yielded reproducible data with a standard deviation of 0.118%

from hundreds of data points. The visually transparent sample became yellowish after irradiation, with transmission spectra showing a drop of 7.8% at 700 nm and a drop of 14.1% at 450 nm, as shown in **Figure 2.1**.

For SrI_2, the energy transition from the ground state to the first excited state of these F-centers is calculated (Knoll, 2010) as $E_{2-1} = 2.47\ eV$ which is 502 nm. From the 425-550 nm range of **Figure 2.1**, the transmission spectra post-irradiation indicates greater absorption compared to 550-700 nm range, a possible indication of F-centers in the sample post-irradiation.

Scintillators may recover from radiation damage due to thermal annealing at room temperature (Zhu, 1998). Repeated transmission spectra were taken on subsequent days to track such recovery, shown in **Figure 2.2**. Although the transmission recovered slightly (0.1%) after the first day, there was a 2% loss in transmission on the second day, followed by another slight recovery (0.2%) the following few days. Transmission worsened the following week, and a possible moisture leak was suspected to be the cause of this transmission loss. Cui et al. provides evidence that I_3^- anions embedded within SrI_2 lattices are the likely hydration species. These anions may be different than free I_3^- radicals or solid I_2, as evidence suggests in previous studies (Cui et al., 2011).

To correct for the suspected moisture leak, the encapsulated sample was stored in a vacuum between measurements and re-pressurized with argon half an hour before each spectrum was taken. A 3% gain in transmission after the first day of vacuum storage is evidence that a moisture leak had been the cause of transmission loss. Recovery tapered off after that, with a 0.2% recovery seen over the next few days, which indicates that a full recovery to pre-irradiation levels may take several weeks or months at room temperature thermal annealing. Recovery speeds depend on the depth of F-center traps formed by the

radiation, so this slow recovery speed suggests deep traps (Zhu, 1998).

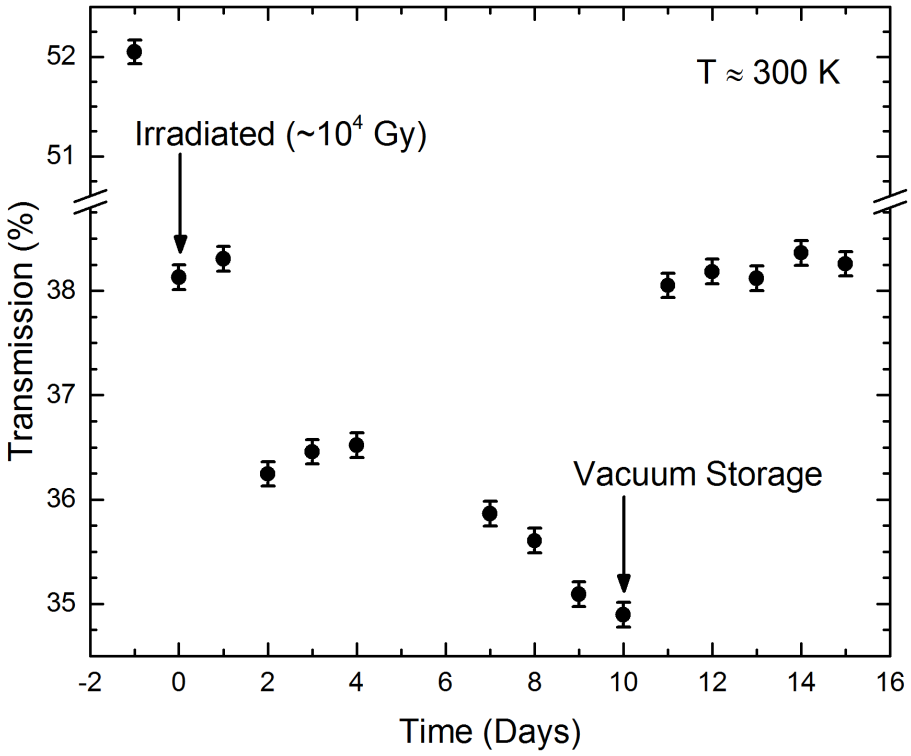

Figure 2.2: Transmission recovery after irradiation (Day 0) at 450 nm at room temperature. First 10 days show a drop in transmission, determined to be a moisture leak in the sealed cuvette. Storing in vacuum between measurements after day 10 and flushing with Ar resulted in a recovery. Note an overall trend of recovery at much less than 1% over 15 days, suggesting slow recovery via thermal annealing at room temperature. Error bars denote the standard deviation at 450 nm of 0.118%.

Scintillation was characterized using a Hamamatsu R6231-100 PMT (photomultiplier tube) with an Ortec Model 556 high voltage power supply, a Hamamatsu C6438 preamplifier, an Ortec Model 671 shaping amplifier, a Picoscope Model 3206A oscilloscope, and a Canberra MP II multichannel analyzer (MCA). Each centroid was calculated using a Gaussian fit. Before each measurement, the sample was wet-polished in light mineral oil to minimize surface effects. During each measurement, the sample was kept in a quartz cuvette filled with light mineral oil, with cuvette coupled to PMT via

silicone optical grease and housed under a light reflector. These steps were taken to ensure sample is free of moisture contamination during gamma spectra measurements. The index of refraction of optical grease and oil is close to 1.5.

Gamma spectra were taken before and after irradiation, as shown in **Figure 2.3**. These spectra were normalized to match the height of the Compton edge. Due to the nonproportionality of the crystal, the Ba K and L peaks differ from their actual values in both spectra, but the post-irradiation spectra show a shift in these peaks, representing a change in proportionality. These Ba peaks arise from the nuclear decay of ^{137}Cs into ^{137}Ba.

The Ba Kα peak, which is a sum of two peaks, Kα_1 and Kα_2, was shifted from 27.8 keV to 32.5 keV (see **Table 2.1** for barium x-ray emissions and their relative intensities). This peak should be approximately 32.1 keV, so the expected light yield was improved from 87% to 101%. The Ba L peak, a summation of 5 peaks averaged to 4.7 keV, was shifted from 16.8 keV to 12 keV. The light yield of the L peak was decreased by 40%, closer to its true value, though 12 keV is still much higher than the actual value of 4.7 keV. As most x-rays around 4.7 keV are absorbed within the first two microns of the crystal, these peaks are particularly susceptible to surface defects.

Shell	*Emission (keV)*	*Intensity per shell*
$K_{\alpha 1}$	**32.194**	**100 %**
$K_{\alpha 2}$	**31.817**	**54 %**
$K_{\beta 1}$	**36.378**	**18 %**
$L_{\alpha 1}$	**4.466**	**100 %**
$L_{\alpha 2}$	**4.451**	**11 %**
$L_{\beta 1}$	**4.828**	**60 %**
$L_{\beta 2}$	**5.157**	**20 %**
$L_{\gamma 1}$	**5.531**	**9 %**

Table 2.1: Barium x-ray emissions, with intensity per shell, where the highest intensity of each shell is listed as 100%. (Adapted from: Bearden, 1967; Krause et al., 1979; Moore, 1970)

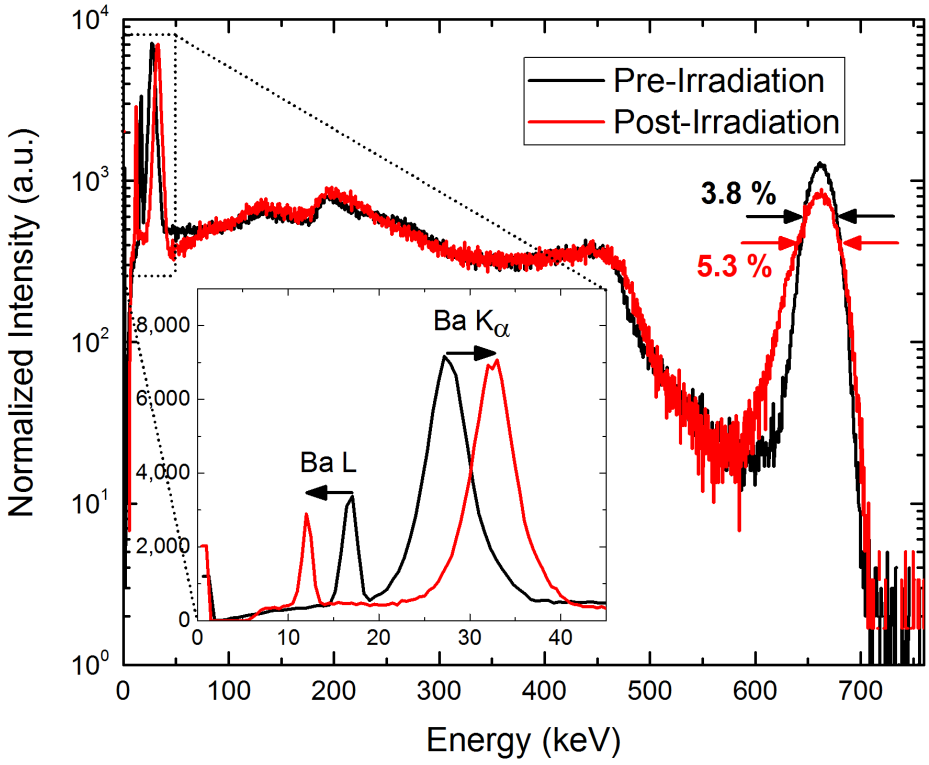

Figure 2.3: Gamma spectra of ^{137}Cs before and after irradiation at 6,200 Gy, with intensity normalized to match the height of the Compton edge. Not only did energy resolution worsen from 3.8% to 5.1%, but the x-ray peaks below 50 keV shifted. The Ba Kα peak shifted right while the Ba L peak shifted left, representing an increase and decrease, respectively, in expected light yield, a shift in the low-energy photon nonproportionality.

The shifts of these two peaks indicate that radiation damage improved the proportionality of the sample, yet the energy resolution worsened. Possibly the reduction in the R_{nPR} term was offset by an increase in the other terms, R_{PMT} and R_{inh}. After radiation damage, the light yield at 662 keV dropped to 48% of the initial light yield. Due to Poisson statistics, this contribution to energy resolution is proportional to $N^{-1/2}$, where N is the number of photoelectrons produced in the PMT (Dorenbos et al., 1995). This means the contribution due to the number of photoelectrons was 144% of pre-irradiated levels, thus worsening the overall energy resolution. An increase in R_{inh} due to increased

inhomogeneity may also be a contributing factor, perhaps caused by the interstitials of the I^- anions created during the formation of F-centers. Though there are no direct data to support this, the contribution due to Poisson statistics for $SrI_2:Eu^{2+}$ is considered to be minimal, thus an increase to 144% may not account for the total worsening of the energy resolution, though it is a contributing factor (Dorenbos 2010). The F-centers may also contribute to reabsorption, further reducing light yield.

For scintillators, there are some differences between electron and gamma nonproportionality at low energies. When a gamma photon is absorbed, creating a hot electron, secondary effects such as Auger x-rays lead to multiple events, compared to the single event of injecting a hot electron directly into the crystal. These differences lead to differing nonproportionality curves (Beck et al., 2015). For either case, the light yield at sufficiently low energies drops below 100%, possibly due to the Birks mechanism becoming the dominant effect on nonproportionality (Payne et al., 2009; Beck et al., 2015). It is unclear why the light yield of the Ba L peak is above 100% in both spectra. Although surface defects dominate in this energy range, the surface was wet-polished before each spectrum to minimize defects. Temperatures did fluctuate by less than 5 ºC between measurements, between 21-25 ºC, but previous studies suggest that temperature variations less than 5 ºC at room temperature should have little to no effect on proportionality (Payne et al., 2014; Perea et al., 2015).

2.4 Conclusions

Radiation damage of $SrI_2:Eu^{2+}$ (2.5%) with a ^{137}Cs source at 6,200 Gy was shown to diminish transmission (-7.8% at 700 nm, -14.1% at 450 nm). Possible recovery of radiation damage by thermal annealing at room temperature was complicated by a suspected

moisture leak, but data suggest that full recovery may take weeks or months. Further research is needed to better quantify recovery rates, although these findings suggest that $SrI_2:Eu^{2+}$ damaged by gamma radiation may recover more slowly than many scintillators used in high-flux radiation environments (Zhu, 1998).

Gamma nonproportionality of the sample was altered by radiation damage, caused by the formation of F-centers that may act in a manner similar to co-dopants. Although a precise nonproportionality curve cannot be established using only three data points, the fact that the 4.7 keV and 32.1 keV peaks shifted in opposite directions is a clear indication that the proportionality of the sample was altered. In the Alekhin and Yang papers (Alekhin et al., 2013a; Yang et al., 2015), changes in nonproportionality were strongest below 100 keV, thus the two low-energy peaks in **Figure 2.3** are good indicators of changes to proportionality. This demonstrates that irradiation may serve as an alternative to co-doping for altering nonproportionality. One possible limitation to this method is room-temperature thermal annealing; as radiation damage recovers over time with a corresponding loss in F-centers, their impact on nonproportionality will diminish. Nevertheless, for the purposes of studying nonproportionality, irradiation may serve as a means of varying proportionality in an otherwise identical crystal.

Energy resolution was, however, worsened by irradiation due to the reduction in light yield. Increased inhomogeneity caused by the displaced ions during the formation of F-centers may have also contributed. Perhaps by limiting the absorbed radiation dose, thereby reducing the number of F-centers formed and maintaining better light yield, nonproportionality may be improved while minimizing this effect.

Work is currently underway to further understand this relationship, including a more robust method of measuring nonproportionality by using a number of gamma sources up to 1.5

MeV, and perhaps varying radiation doses and quantifying their impact. Recovery time is also being further investigated with enhanced encapsulation methods to avoid any future issues with moisture leaks.

CHAPTER 3

MANIPULATING NONPROPORTIONALITY OF STRONTIUM IODIDE CRYSTALS WITH HIGH-FLUX IRRADIATION BY ^{137}CS GAMMA RAYS

Here we expand and adapt from work submitted to the Nuclear Instruments and Methods in Physics Research A on January 30, 2017.

3.1 Abstract

Strontium Iodide ($SrI_2:Eu^{2+}$) crystal scintillators are being developed for gamma detectors due to their high light yield and superior energy resolution that is primarily limited by nonproportionality. Only in the past few years have the underlying physical models of nonproportionality been reported. Materials science solutions for improving nonproportionality are also being investigated, with the main approach being the incorporation of deliberate addition of crystal defects using codoping. In this study, we look at an alternative method that is similar to codoping, using radiation damage to alter proportionality. The $SrI_2:Eu^{2+}$ scintillators were exposed to 1,000 Gy(SrI_2) dose induced by exposure to a 2,222 Ci ^{137}Cs source. After irradiation the crystal transmission spectral intensity was reduced by 8.0% at 700 nm and 23.6% at 450 nm. Over two months, transmission spectra returned to pre-irradiation levels at a rate of approximately 0.1% per day via room-temperature thermal annealing. Nonproportionality was also altered after irradiation, and sequentially worsened, then improved over pre-irradiation levels as the samples recovered. This demonstrates that radiation damage is an effective approach for defect engineering that may be used to study nonproportionality in scintillators. The advantage of this proposed approach is that one can use the same crystal to vary the

concentration of defects, while codoping introduces additional variables, since it requires growing a different crystal for each codoping concentration.

3.2 Introduction

Many phenomena in the universe, such as pulsars, quasars and black holes, cannot be detected except in the x-ray and gamma-ray regimes. As these objects are far away, typically in distant galaxies, these sources are very weak to observers. Gamma ray spectrometers used to detect weak sources require detector materials that have superior energy resolution, to resolve signal over noise, and can be cheaply grown to large volumes, to maximize the capture of gamma rays. Strontium iodide, in particular, shows great promise (Cherepy et al., 2009a; Cherepy et al., 2009b; Cherepy et al., 2008). Nonproportionality in scintillators broadens energy resolution, and is the primary limiting factor for energy resolution for halides such as strontium iodide (Dorenbos, 2010), yet the processes that affect nonproportionality are not well understood. Some recent papers have shown a correlation between improving proportionality and energy resolution through the use of codopants (Alekhin et al., 2013a; Alekhin et al., 2013b; Yang et al., 2015). In our previous work (Caudel et al., 2016), we proposed an alternative to codopants – radiation damage – as a tool for studying nonproportionality and its impact on energy resolution.

Radiation damage in scintillators is predominantly expressed in the formation of color centers (F-centers), where ions are displaced in the lattice, leaving a negatively-charged vacancy – an induced trap. When an electron becomes trapped in this vacancy, it may be excited from its ground state, behaving like a codopant. Thermal annealing at room temperature will return displaced ions to such vacancies, often over days, weeks or months, with longer recoveries attributed to deeper induced traps (Zhu, 1998).

Energy resolution is given by the equation

$$R^2 = R_{PMT}^2 + R_{inh}^2 + R_{nPR}^2, (1)$$

where R_{PMT} is due to the process where light is captured from the scintillator (transfer of photons from the crystal to the PMT, gain and Poisson statistics); R_{inh} is due to inhomogeneities in the crystal, typically defects produced by crystal growth; and R_{nPR} is due to the nonproportional response (Dorenbos et al., 1995). For strontium iodide, nonproportionality is calculated to be the dominant effect limiting energy resolution, with the R_{nPR} term equal to or greater than the first two terms (Cherepy et al., 2009b).

As F-centers may affect nonproportionality in a manner similar to codopants, and thermal annealing at room temperature reduces the number of F-centers over time, these effects result in dynamic proportionality. Thus, nonproportionality may be studied in the same crystal as the F-centers diminish. For strontium iodide, previous work suggested a slow recovery rate, suggesting a slow shift in nonproportionality over time (Payne et al., 2009).

The impact of nonproportionality on energy resolution is an active area of research (Payne et al., 2009) (Payne et al., 2011) (Payne et al., 2014) (Beck et al., 2015). In a model of competing influences that impact nonproportionality, the Birks mechanism is used to consider exciton-exciton annihilation and other exciton and carrier losses. The Birks mechanism may become the dominant term impacting proportionality in the lower energy regime (Payne et al., 2009).

This study builds upon Chapter 2 (Caudel et al., 2016) using high-flux ^{137}Cs gamma rays to induce radiation damage to $SrI_2:Eu^{2+}$ samples and assess the changes to the transmission spectra and gamma spectra. Multiple radiation sources were used to obtain a better understanding of the nonproportionality shifts. Transmission recovery is also more definitively explored.

3.3 Experimental Results

Samples were harvested from a SrI_2:Eu^{2+} (2.5%) boule grown at Fisk University using the vertical Bridgman method and cut and wet-polished (up to 1200 grit) to dimensions of approximately $9\times8\times7\ mm^3$. Two samples were used, designated as APL1 and APL2. APL1 was used to obtain gamma spectra, while APL 2 was used for transmission spectra. In this manner, radiation damage recovery was assessed in tandem. Both samples were compared prior to irradiation to ensure matching characteristics. Irradiation was performed using a Shepherd Mark I Cesium-137 Irradiator Model 68, which was commissioned in September 1981 with a 5,000 Ci ^{137}Cs source. With a half-life of 30.17 years (Unterweger et al., 2010), the activity of the source was calculated to be 2,222 Ci during the experiment. The samples were hermetically sealed in quartz during the irradiation. The crystals were sealed in an argon atmosphere rather than immersed in light mineral oil, to avoid any possible interactions between oil/surface and irradiation. The irradiator dose rate was calibrated and calculated by the same methods as in ref. Caudel et al., 2016. The samples were irradiated to produce a dose of 1,000 Gy(SrI_2).

Optical transmission spectra were performed using a Varian Cary 500 Scan UV-Vis-NIR Spectrophotometer with a quartz holder filled with light mineral oil used as a baseline. Each quartz container was filled with light mineral oil that was heat-treated, rather than argon as in previous work (Caudel et al., 2016), and stored in a desiccator to minimize moisture contamination. Also, sealed cuvette was used for irradiation only. Prior to irradiation, both samples were tested over several days and showed no degradation of transmission under these conditions, so no hydrate formations were detected. These steps were taken to avoid the suspected moisture leak seen in previous work (Caudel et al., 2016).

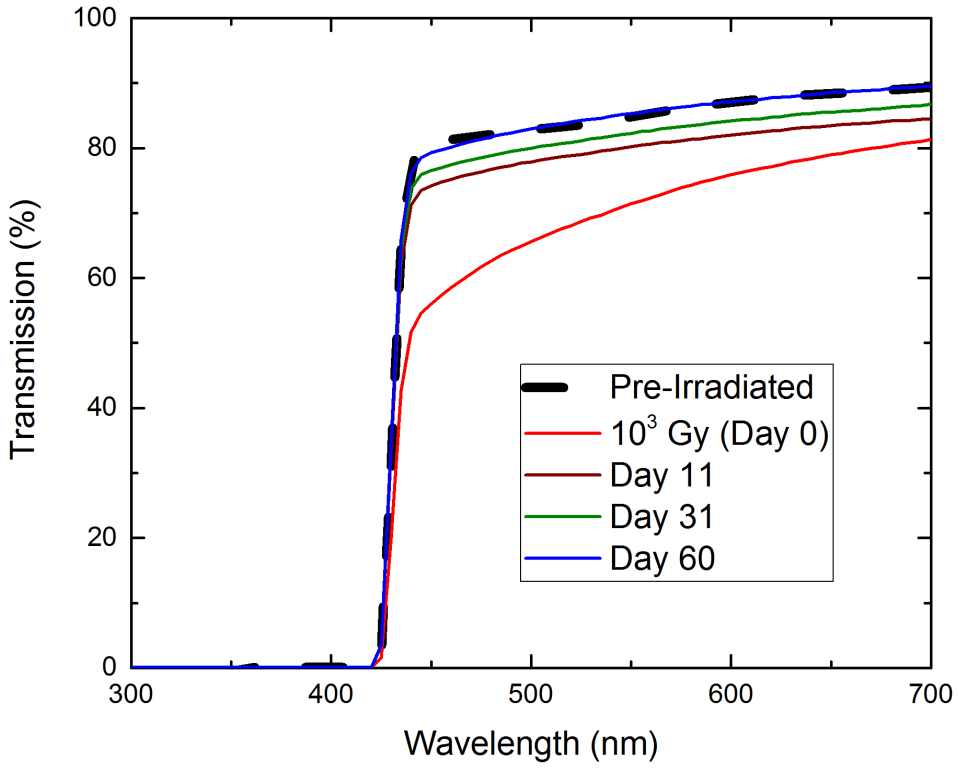

Figure 3.1: Comparison of optical transmission spectra before and after 1,000 Gy(SrI_2) (^{137}Cs source) irradiation of $SrI_2:Eu^{2+}$. Note a trend of full recovery within 60 days via room-temperature thermal annealing.

After irradiation to a dose of 1,000 Gy(SrI_2), visually clear samples appeared yellowed, as in Chapter 2 (Caudel et al., 2016), and transmission spectra dropped 8.0% at 700 nm and 23.6% at 450 nm, as shown in **Figure 3.1**. The slope of the transmission spectra from 450-700 nm increases after irradiation, leading to a much larger drop in transmission at 450 nm compared to 700 nm. By 11 days post irradiation, the slope receded to pre-irradiation levels and transmission steadily improved until the signal intensity had fully recovered within 60 days via room temperature thermal annealing, at a rate of 0.098% per day at 700 nm and 0.094% per day at 450 nm. This is consistent with previous work, and indicates that the F-center traps formed by radiation damage in $SrI_2:Eu^{2+}$ are deep

(Zhu, 1998).

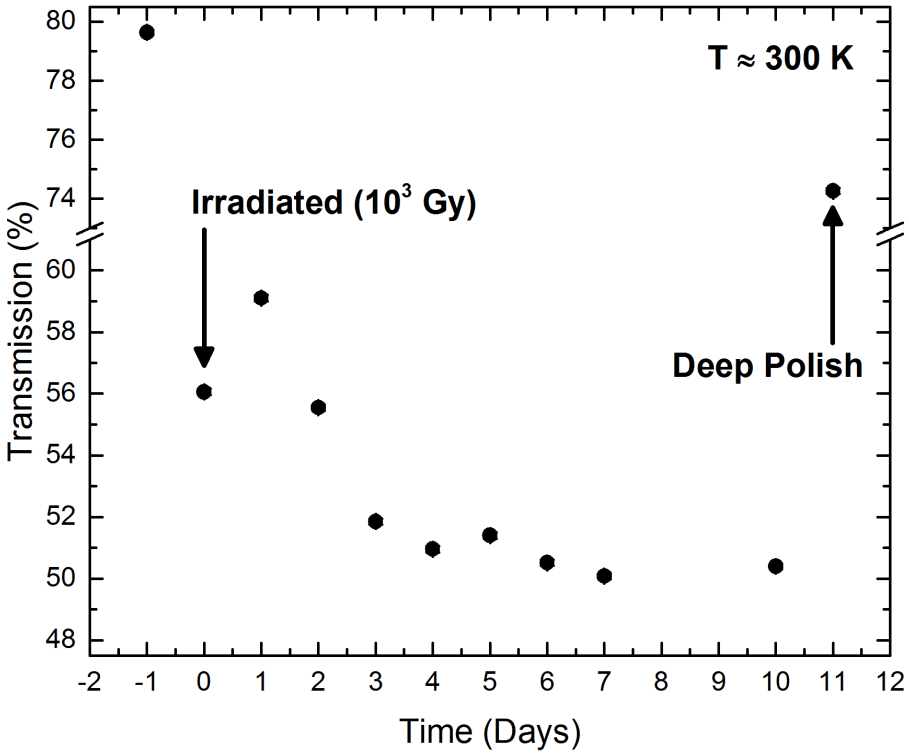

Figure 3.2: Transmission recovery after irradiation (Day 0) at 450 nm at room temperature. First ten days show a drop in transmission which stabilizes by Day 7 around 50%. Sample was polished on Day 11, removing roughly 50 microns of each surface, noted as "Deep Polish" in the graph. From Day 11 on, sample showed a steady improvement as illustrated in **Figure 3.1**.

Transmission intensity deteriorated after irradiation, in a manner similar to previous work, as seen in **Figure 3.2**. As this effect is reproducible in the absence of hydrate species, a moisture leak is no longer suspected as previously thought. Instead, radiation damage near the surface may be the cause of this effect. In addition to 662 keV gamma rays, the interaction of ^{137}Cs with the surrounding walls and shielding materials generates low-energy secondary electrons that are efficiently absorbed at the surface of the crystal (Kerris et al., 1985; Fleetwood et al., 1988). A deep polish on day 11, removing roughly 50

microns of each surface of the sample, eliminated these defects. The sample was kept in desiccated, heat-treated oil for the next 50 days with no further polishing, and recovered to pre-irradiation levels with no evidence of hydrate formation.

Scintillation characterization was performed using a Hamamatsu R6231-100 PMT (photomultiplier tube) with an Ortec Model 556 high voltage power supply, a Hamamatsu C6438 preamplifier, an Ortec Model 671 shaping amplifier, a Picoscope Model 3206A oscilloscope, and a Canberra MP II multichannel analyzer (MCA). Each centroid was calculated using a Gaussian fit. Before each measurement, each sample was wet-polished in light mineral oil to minimize surface effects. During each measurement, the sample was kept in a quartz cuvette filled with light mineral oil, with the cuvette coupled to the PMT via silicone optical grease and housed under a light reflector. The index of refraction of optical grease and oil is close to 1.5. Average decay time of gamma spectrum pulse was measured using ^{137}Cs source before and after irradiation, and throughout recovery, but no statistically significant change was measured.

Gamma spectra of a ^{137}Cs source (10 μCi) were used to assess the impact of the radiation damage on energy resolution, specifically the 662 keV peak. Each peak was fitted to a two-peak Gaussian to measure both the 662 keV peak and any defect or secondary peaks. As seen in **Figure 3.3**, for the pre-irradiation sample, no defect peak is detected – a very faint secondary peak around 629 keV is consistent with an iodine escape peak. As these samples are approximately 7 mm thick, few x-rays would escape, so little or no escape peak was to be expected. The pre-irradiation secondary peak makes up less than 4% of the peak signal.

The post-irradiation characteristics show a large defect peak demonstrated by the two-peak fit. As a deep polish on day 11 did not impact the rate at which the defect peak

diminished, and most scintillation events happen away from the crystal surface, this peak is attributed to defects present in the bulk of the crystal. At day 0, the defect peak comprises 36% of the overall signal. It makes up 23% on day 3, 22% on day 7, 10% on day 14 and 7% by day 18. By 24 days after irradiation, the secondary peak was reduced to pre-irradiation levels, where it remained.

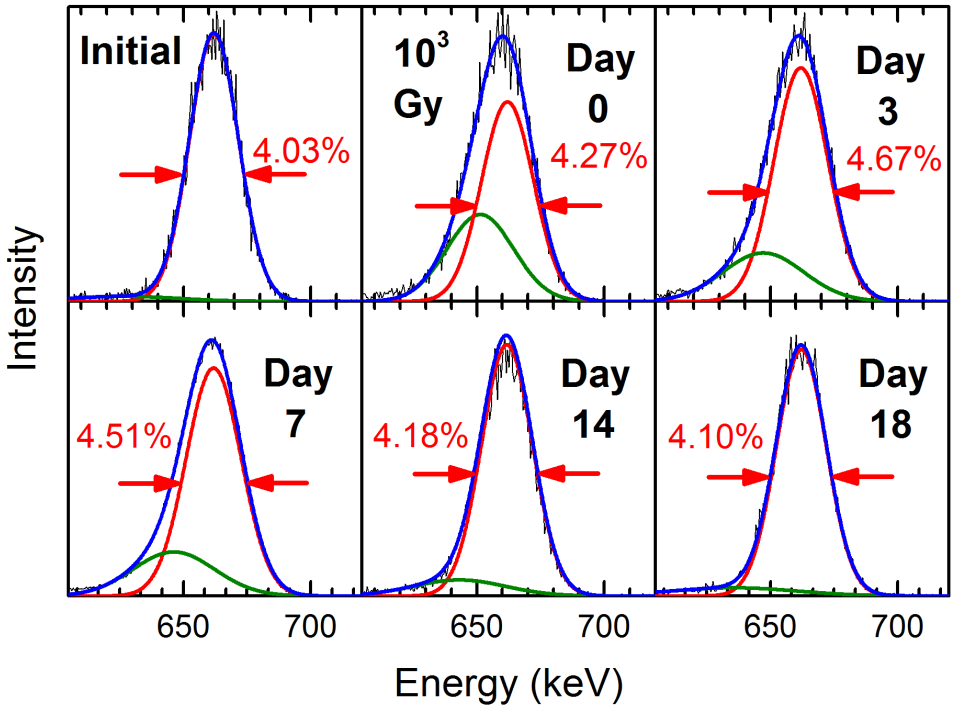

Figure 3.3: Gamma spectra of ^{137}Cs 662 keV peak before and after 1,000 Gy(SrI_2) of irradiation. Each peak was fitted to a two-peak Gaussian: blue indicates composite peak, red the 662 keV peak, and green the defect or escape peak. Initial represents pre-irradiation peak, then at Day 0 the sample was irradiated to 1,000 Gy(SrI_2). Note the large defect peak on Day 0, diminishing to Day 18. After Day 24, each green peak remained at pre-irradiation levels. Energy resolution is given in percentage, with FWHM marked with red arrows.

For each two-peak fit, the 662 keV component was also analyzed for energy resolution. **Figure 3.4** illustrates the shift in energy resolution as the sample recovered from radiation damage. For the first week after irradiation, energy resolution worsened from pre-irradiation of 4.03% (±0.05%) to approximately 4.6%, corresponding with the

large defect peak noted in **Figure 3.3**. As the defect peak diminished, energy resolution improved, and by day 20 was at pre-irradiation levels. By day 24, however, energy resolution worsened, climbing to 4.95% (±0.05%) by day 60, an increase of +0.92% over pre-irradiation levels.

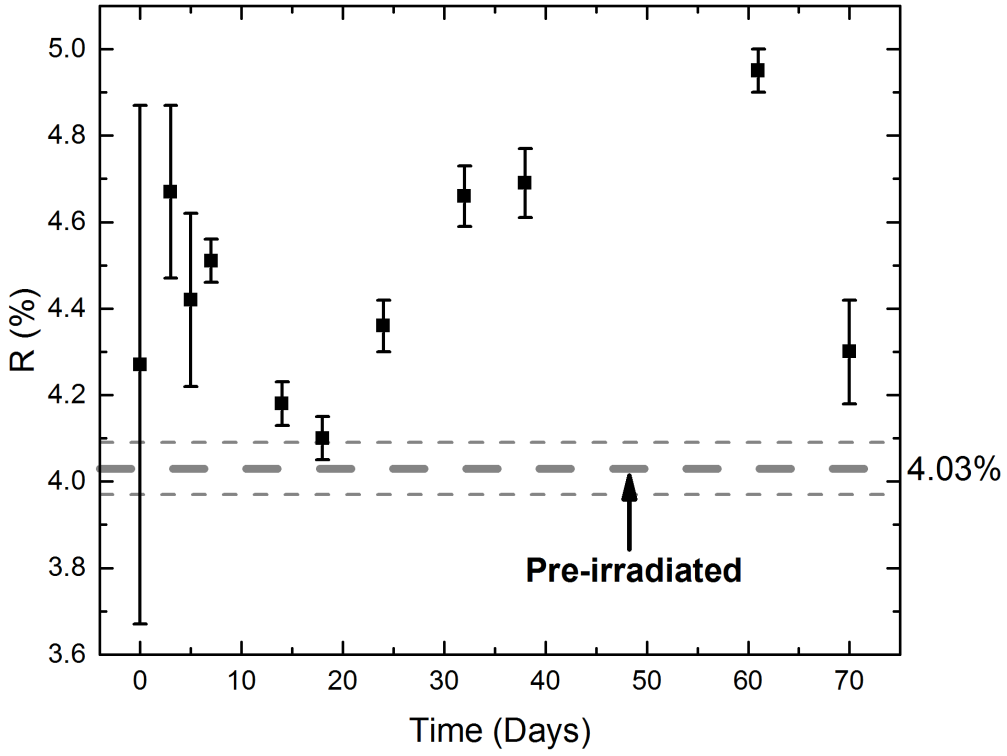

Figure 3.4: $SrI_2:Eu^{2+}$ energy resolution of the 662 keV peak after 1,000 Gy(SrI_2) of irradiation. The dotted line at 4.03% represents the energy resolution prior to irradiation. Error bars were obtained via the standard deviation of each Gaussian fit. Note on Day 18 energy resolution was nearly at pre-irradiation levels, coinciding with disappearance of defect peak seen in **Figure 3.3**.

To further explore the impact of radiation damage, light yield was calculated by taking each channel number of the 662 keV centroid and expressing as a pre-irradiation percentage. In **Figure 3.5**, light yield drops by nearly 10% in the first week after irradiation. Although there is a positive trend in the first month, by day 30 the recovery

plateaued at approximately 5% below pre-irradiation levels.

Nonproportionality characterization was performed using the scintillation setup, detailed above, with a variety of gamma sources: ^{57}Co, ^{109}Cd, ^{133}Ba, ^{22}Na, and ^{137}Cs. Two spectra were taken for each data set: one for ^{137}Cs and a combined spectra for the remaining data points.

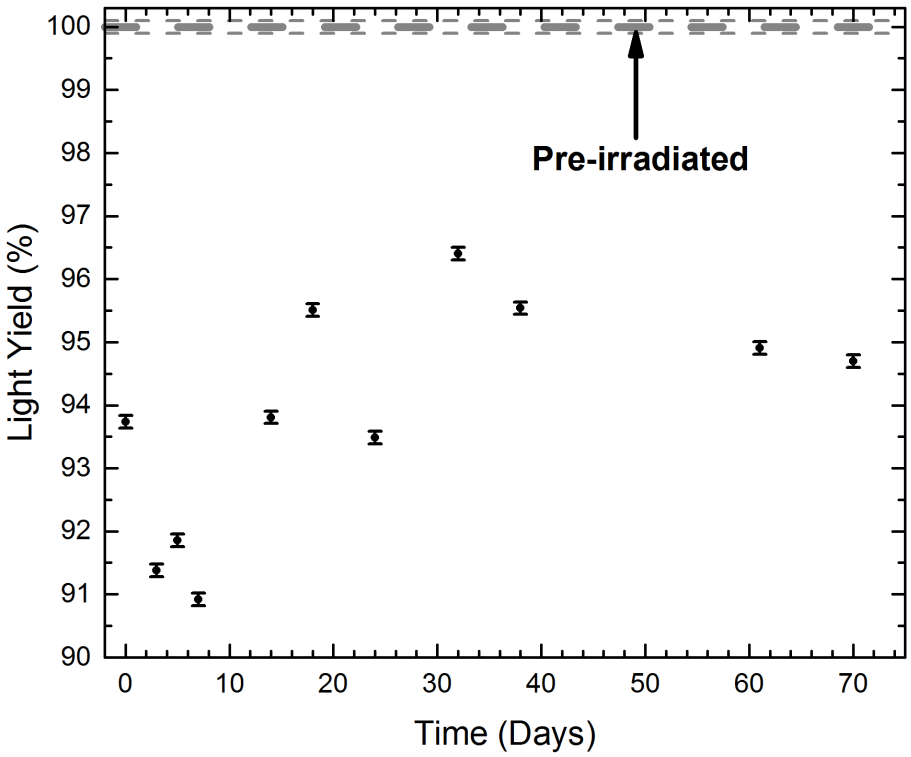

Figure 3.5: Light Yield recovery of ^{137}Cs 662 keV peak after irradiation at 1,000 Gy(SrI_2), with 100% representing the pre-irradiation channel centroid. Error bars denote standard deviation of the centroid fit.

Radiation damage altered the nonproportionality of the samples, as seen in **Figure 3.6**. After irradiation, the nonproportionality curve dropped below pre-irradiation levels. During the first week, this improved, nearing normal levels, and by day 18 the nonproportionality curve had risen above pre-irradiation levels, signifying heightened light

yield below 662 keV. Each curve followed a similar trajectory with little deviation. These trends are well represented by plotting the scintillator response at 122 keV in **Figure 3.7**. Scintillator response is analogous to the relative light yield. One possible explanation of these trends is the Birks mechanism (Payne et al., 2009) – the F-centers may be at times aiding or hindering exciton-exciton annihilations and/or carrier losses, depending on the density of the F-centers.

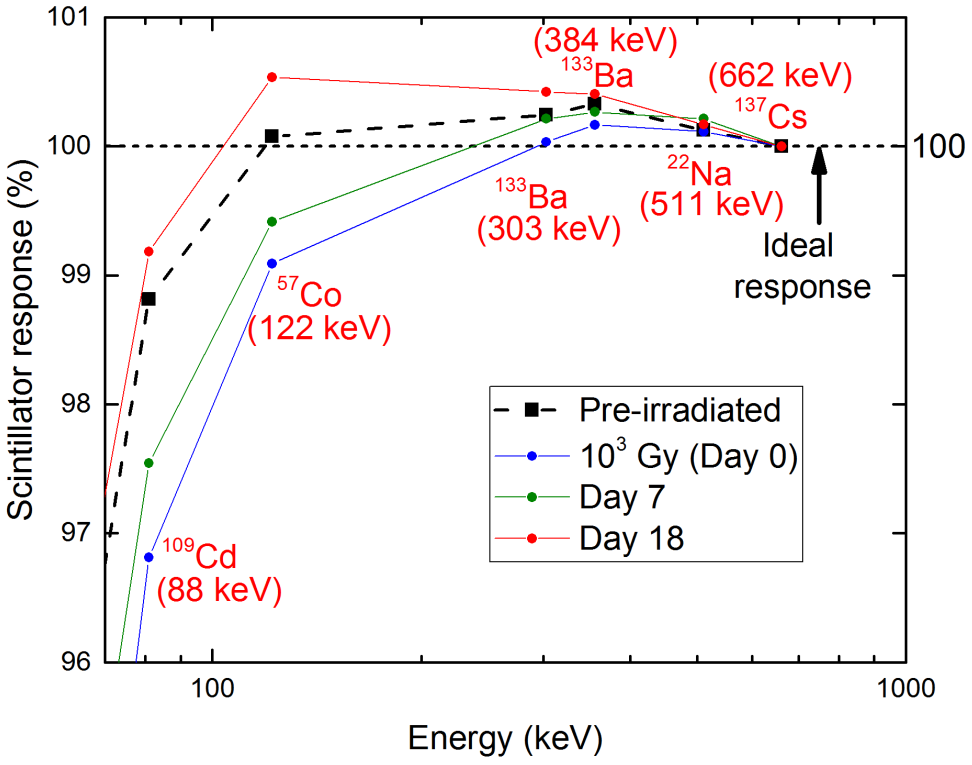

Figure 3.6: Nonproportionality of $SrI_2:Eu^{2+}$ during recovery from 1,000 Gy(SrI_2) dose. Scintillator response is the relative light yield, where 100% is the proportional response. Each curve is normalized at 662 keV. The error is 0.1-1% depending on the energy.

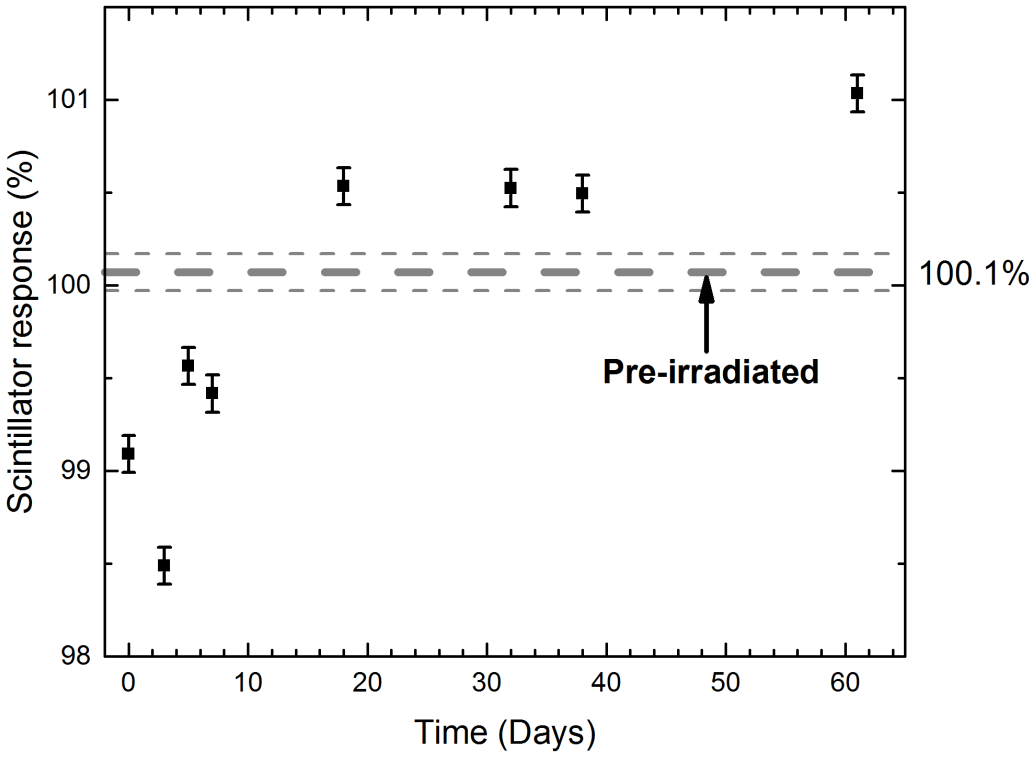

Figure 3.7: Nonproportionality of $SrI_2:Eu^{2+}$ at 122 keV during recovery from 1,000 Gy(SrI_2) dose, with dashed line representing pre-irradiation level at 100.1% of ideal response. Error bars denote standard deviation of the centroid fit.

On day 3 after irradiation, energy resolution was 4.67% (±0.2%), much worse than the pre-irradiation energy resolution of 4.03 (±0.06%). The contribution to energy resolution, R_{PMT}, is proportional to $N^{-1/2}$, where N is the mean number of photons captured by the PMT from the scintillation event (Dorenbos et al., 1995). Therefore, a loss in light yield equals a corresponding degradation of the energy resolution. On day 3, the light yield was 91.38% of pre-irradiation levels. Reducing N by this amount, the R_{PMT} term becomes 104.6% of the original value, increasing its contribution to resolution. Although the defect peak illustrated in **Figure 3.3** had already diminished at this point compared to day 0, it was still substantial, comprising 23%, compared to 4% of the pre-

irradiation value. This indicates that the inhomogeneities were much greater than pre-irradiation levels, so it is reasonable to assume that R_{inh} was also increased. Finally, there is a greater loss in light yield at low energies on day 3, as seen in **Figure 3.7**, where the scintillator response is at its lowest point in the study. This indicates that the third term, R_{nPR}, also increased because the nonproportionality was larger than pre-irradiation levels. Thus, all three terms contribute to broadening of the energy resolution, consistent with the increase of +0.64% seen on day 3. Further, it is reasonable to assume that R_{inh} grew substantially more than R_{PMT}, given that R_{PMT} was only 104.6% of pre-irradiation levels and such a large defect peak was present.

On day 18 after irradiation, energy resolution was 4.10% (±0.05%), close to the pre-irradiation energy resolution of 4.03 (±0.06%). The light yield was 95.4% of pre-irradiation levels. Reducing N by this amount, the R_{PMT} term becomes 102.4% of the original value. Although the defect peak illustrated in **Figure 3.3** had largely diminished at this point, it was still detectable, comprising 8%, compared to 4% pre-irradiation. This indicates that the inhomogeneities were still much greater than pre-irradiation levels, so it is reasonable to assume that R_{inh} was also increased. If both the energy resolutions of day 18 and pre-irradiation are assumed to be equal (errors overlap), then the increases in R_{PMT} and R_{inh} would need to be offset by a decrease in R_{nPR}. **Figure 3.6** shows a rise in the nonproportionality curve at lower energies, consistent with a decrease in R_{nPR}.

From day 31 on, a new trend emerged that contradicts these conventions. Energy resolution continues to rise to 4.95% (±0.05%) by day 61, yet no defect peak is detected to affect inhomogeneities and nonproportionality remains at or better than pre-irradiation levels. Light yields also remain at about 95%. Perhaps as the interstitials migrate and F-

centers diminish, they aid proportionality while also increasing the R_{inh} term with inhomogeneities not detectable via a defect peak. As comparisons between shifting light yield and nonproportionality may be measured but the migration of these defects cannot, this cannot be verified in this study, though it seems the most plausible explanation to these trends.

3.4 Conclusions

Using ^{137}Cs source at 1,000 Gy(SrI_2), radiation damage of SrI_2:Eu^{2+} was shown to reduce transmission by -8.0% at 700 nm and -23.6% at 450 nm when measured in light mineral oil. Full recovery of transmission took approximately two months, at a rate of approximately 0.1% per day, consistent with previous work in Chapter 2 that suggested that these halides recover more slowly than most scintillators (Caudel et al., 2016).

For the first 10 days after irradiation, transmission spectra did not recover as expected, but decayed in a manner consistent with previous research (Caudel et al., 2016). A deep polish, removing approximately 50 microns of each surface, improved transmission by +23.9% at 450 nm, eliminating any further decay. In previous work, a moisture leak was hypothesized to be the cause of this decay, but data presented here shows that this effect is reproducible in the absence of moisture and suggests that low-energy secondary electrons from the ^{137}Cs source may have been the cause of transmission decay – under room-temperature thermal annealing, these surface defects may have migrated, combined, or neutralized over time, impacting the transmission spectra. After polishing the surface of the crystals, no further decay was detected. Therefore, a deep polish is recommended after irradiation to remove these surface effects. Low-energy shielding may also be considered during irradiation, such as an aluminum lead-lined box that could attenuate the x-rays with

negligible moderation of the 662 keV gamma rays (Kerris et al., 1985; Fleetwood et al., 1988).

For the first two weeks after irradiation, a large defect peak was present at 662 keV. This peak was strongest the day of irradiation, and diminished over successive days via room-temperature thermal annealing. Displaced ions from radiation damage may be the cause of this defect peak. Such ions may become interstitials, warping the lattice around them. As the defects in the crystal are significantly increased, this would increase the R_{inh} term due to inhomogeneities, further complicating study of nonproportionality via radiation damage. This defect peak diminished over time and was no longer detectable by day 24.

Proportionality worsened after irradiation on day 0, then improved until rising above pre-irradiation levels as the crystal recovered from radiation damage via room-temperature thermal annealing. The data suggest that, as displaced ions migrate and return to fill induced traps, eliminating the F-centers formed by the radiation damage, the changing densities of defects, traps and F-centers hinder or aide exciton-exciton annihilation and carrier losses, depending on the density. Thus, a variety of densities and their impact on nonproportionality may be studied by this method.

In future work, radiation damage in strontium iodide via a proton source will be investigated. As these detectors may one day be used in space-based applications, where they would be subjected to cosmic radiation, proton irradiation would be a better simulate of conditions in space.

3.5 Acknowledgements

The authors would like to express their sincere thanks to Vladimir Buliga for his help with encapsulation and to Pijush Bhattacharya for advice on encapsulation methods.

CHAPTER 4

FUTURE WORK

4.1 Cosmic Radiation

Galactic cosmic rays are mostly subatomic particles: atomic nuclei, ionized protons, and beta particles (electrons). Approximately 90% of cosmic rays are protons (ionized hydrogen) and about 9% are alpha particles, or ionized helium nuclei (NASA, 2010b). Although the source of cosmic rays are not fully understood, particles measuring up to 10^{20} eV have been detected, consistent with some proposed models of galactic and intergalactic sources (Biermann et al., 2012). Cosmic rays are the primary source of radiation in space and, potentially, radiation damage to satellite detectors. In this work, we used gamma radiation damage to simulate cosmic ray damage to our devices. Previous studies showed high-flux gamma irradiation damage to be a good predictor of how well CMOS devices behave in space-based environments (Winokur et al., 1986), yet gamma radiation, composed of photons, differs from cosmic radiation, which is composed of high-energy subatomic particles. A proton source will be used to simulate cosmic rays and induce radiation damage and compare that to this work.

4.2 Switching from Gamma to Proton Source

In future work, the effects of high-energy proton particle damage to strontium iodide samples will be examined, comparing the results to those in Chapters 2 and 3, focusing on the impact to nonproportionality and energy resolution. Several samples of $SrI_2:Eu^{2+}$ harvested from the same boule have been selected and the energy resolution and nonproportionality of each sample measured. Samples will be shipped to Loma Linda

University (LLU), to be exposed to a proton beam from their accelerator, one set below 50 MeV, another set around 200 MeV, at variable doses.

As cosmic rays are composed mostly of high-energy protons (90%), it is reasonable to assume that a proton accelerator would produce a better simulated space irradiation environment than high-flux gamma rays, though there are some limitations to this thinking. The proton accelerator at LLU, in fact any accelerator on earth, can match only a fraction of the energy of many cosmic rays. Despite this limitation, this study may render a more complete understanding of how well this material would function in space-based applications. Also, even 2 MeV protons should be capable of penetrating the 1-cm^3 samples, given that 2 MeV protons can penetrate approximately 10 cm of tissue, though to what degree and what fraction would completely pass through the material is currently being calculated.

Low-temperature thermal annealing will also be investigated to determine the rate of recovery from proton radiation damage. A target temperature of 100^o-150^o C is planned, to simulate space-based conditions: in satellites, such annealing temperatures are feasible for onboard systems.

CHAPTER 5

BOLD FELLOWSHIP

5.1 Online Content

Throughout graduate work while training several students and faculty on the use of the Atomic Force Microscope (AFM) in Dr. Burger's group at Fisk University, a need for an instructional video was determined, so a simple 10-minute introduction into the proper use of the AFM was designed, edited and published, made publicly available on YouTube (Caudel, 2013). As of March 2017, this instructional video as had over 33,000 views and has become a standard part of training for this device.

In 2014, I was accepted to the Blended & Online Learning Design (BOLD) Fellows Program, a one-year fellowship designed to help graduate student/faculty teams build expertise in developing online instructional materials grounded in good course design principles and the understanding of how people learn (Brame, 2017). Teaming up with faculty, an online course was built to teach celestial navigation, also known as astronavigation, free and open to the public (Caudel et al., 2015). This online course is a self-sustained, 2-hour primer on the basics, with 15 videos, each with an interactive "Test Your Understanding" quiz for formative assessment. In 2016, we learned that the U.S. Navy now includes this online course in training naval officers, and it has become a standard part of their curriculum.

5.2 Astronavigation

Before the wide-spread use of the Global Positioning System (GPS), celestial navigation was the primary means of determining the position of ships as they navigate

oceans. Using a sextant, the visible horizon, celestial bodies, time, published tables, and simple math, this system has allowed navigators to chart their courses for centuries. With the advent and widespread use of GPS, classes that taught celestial navigation diminished, and today few course are available to the public. Since electronic systems may fail and some navigators may wish to have a backup means of finding their location, we decided to build a free, online course as part of the BOLD program to teach the basics of celestial navigation to the public. This course was also used in the Vanderbilt undergraduate astronomy lab to familiarize students with celestial navigation, and was stress-tested by the Navy ROTC at Vanderbilt.

5.3 Preparation

The BOLD program teaches course design and processes at each stage, how to examine pedagogical choices, online learning techniques, and the creation of products that benefit students in targeted classes. Typically, the BOLD fellow is teamed with a professor to augment the lecture, focusing on a particular topic or subject that the professor has identified as a subject that many students struggle to master. These topics become the focus of the online content, through animated, instructive videos, as a learning tool the professor may then use to help the students to better understand the lesson.

Before we could build an online course to teach celestial navigation, we first had to learn the subject ourselves, so we reached out to the Annapolis School of Seamanship in Maryland. Ralph Naranjo, a retired instructor, agreed to leave retirement and teach us the basics of celestial navigation. After this week-long course, contact was maintained with Naranjo, who verified the accuracy of each topic taught in the videos and was a tremendous help as a subject-matter expert in the field.

I also procured free software online to create and edit the videos, used Microsoft PowerPoint to create animations, and published the content on YouTube, linking the videos to the content website (Caudel et al., 2015). An example of a course page is shown in **Figure 5.1**.

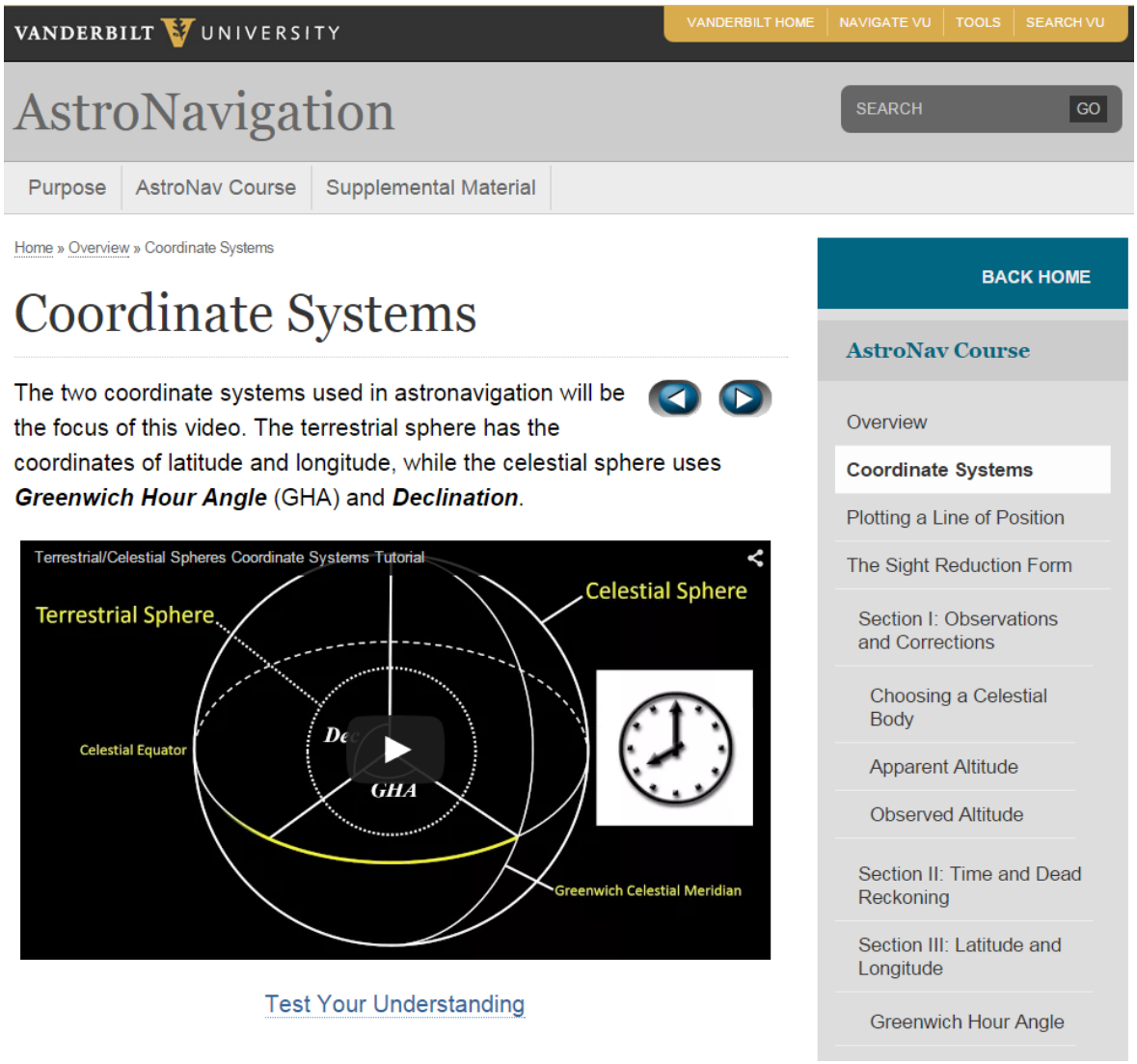

Figure 5.1: Example of the online course on celestial navigation, also known as astronavigation. The interactive video is linked to a YouTube account for ease of navigation through the course, while the "Test Your Understanding" link takes the students to an interactive set of questions – formative assessment intended to reinforce the topics covered in each video. (Caudel et al., 2015)

5.4 Course Design

Although celestial navigation uses spherical trigonometry to track celestial bodies and their locations on earth (by assuming the zenith, or where the object is directly overhead, as the terrestrial location) and then triangulates position with two or more fixed points in time, the complicated math involved is reduced to a simple set of tables published by the U.S. Naval Observatory and their UK partners. In order to use these tables, navigators use the Sight Reduction Form, a worksheet that walks them through what tables to use to calculate their position. As understanding this form is key to using celestial navigation, we decided to focus the course on completion of this form, using the sun as an example.

Although there are a number of Sight Reduction Form templates, we felt we could improve upon these designs, so we created one tailored to our lesson. Feedback from students indicated they found this form easier to use compared to earlier forms.

As a self-contained course, care was taken to ensure students could reasonably complete the work with no guidance from an instructor. For background knowledge, we did a few videos explaining topics such as an introduction to celestial navigation, coordinate systems used for celestial and terrestrial bodies, and some basics to plotting a course at sea. As the sight reduction form has four sections, each with a number of steps, we did a separate video on each step. We also included a “Test Your Understanding” quiz for each video, a set of questions designed to reinforce each lesson taught. A correct answer would return an explanation of why it was correct, and an incorrect answer would explain why the answer was wrong and allow students to answer the question again. Known as formative assessment, these quizzes were not intended to grade the students, but rather to help them reinforce and remember every lesson taught in each video. To make

this process feasible, each quiz takes the form of multiple choice, with care taken that each incorrect answer would be a reasonable guess for students who were uncertain. As each student completes a quiz, data is sent back to us to assess how effective each lesson was. Finally, a collection of supplemental resources were included for any questions beyond the scope of this course.

5.5 Feedback

In spring of 2015 at Vanderbilt University, undergraduates in the astronomy labs and students from the Navy ROTC took the course. Data shows that, among the formative assessment quizzes, students guessed correctly on their first attempt from 61.6% on the most difficult parts to 86.0% on the easiest parts. Students were also given a survey at the end of the course. When asked, "do you feel that this online course helped you to understand what astronavigation is used for," 92.2% said yes, 1.6% said no, and 6.3% were undecided. When asked, "do you now have a good sense of how to use astronavigation," 62.5% said yes, 12.5% said no, and 25% were undecided. Students were also encouraged to leave comments, suggestions, and to complete a questionnaire. Some of these survey results are shown in **Figure 5.2**.

We examined the data, making some changes and clarifications to the materials to improve lessons that had a lower score. Trends in the student feedback were also considered in these changes. Once completed, we made the online course open to the public, adding search engine keywords to maximize discovery by anyone with an interest in this topic.

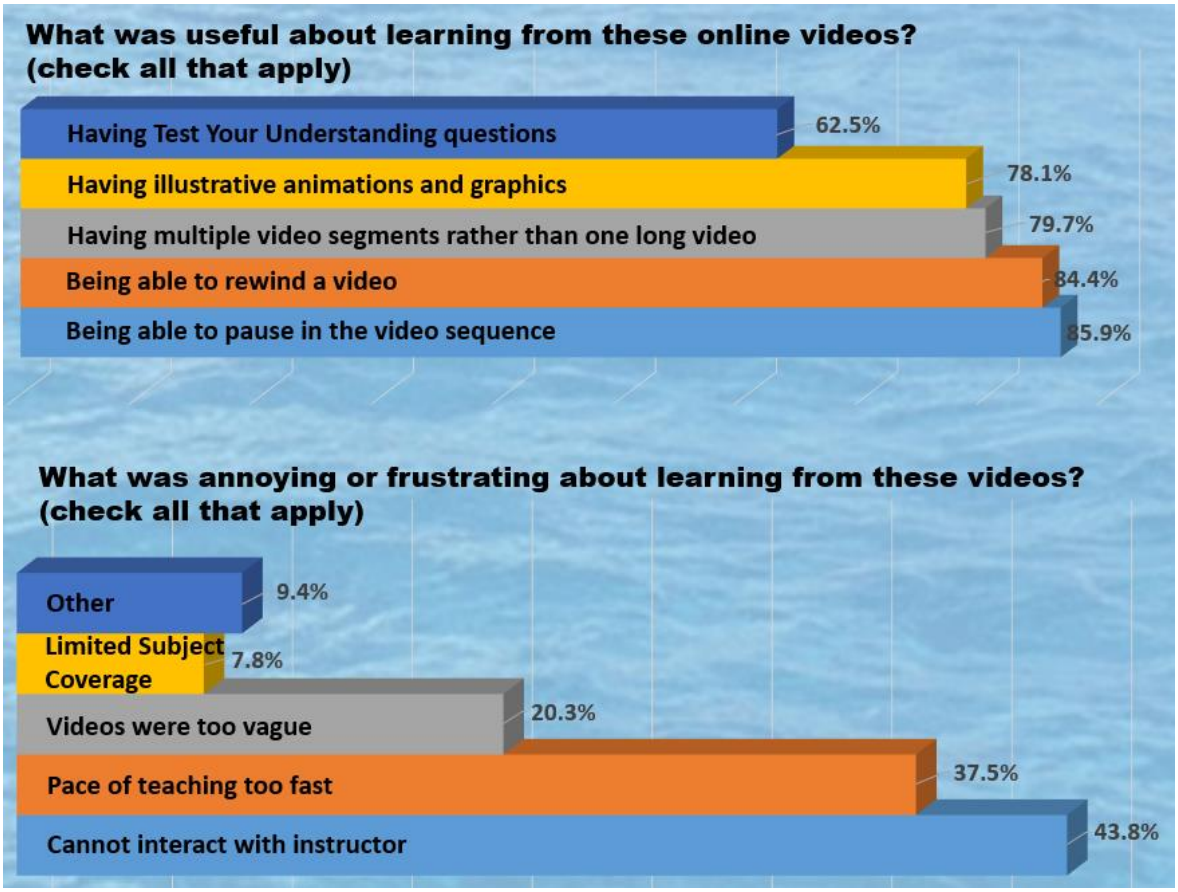

Figure 5.2: Survey results from spring 2015 rollout. (Caudel et al., 2015)

As of January of 2017, we had 963 students register to fully participate in the course. For 2016, our most popular video had 14,582 unique views and our videos had a combined 48,313 unique page views. In 2016, we also received word from the U.S. Navy that as of the summer of 2016, this online course is now used to train naval officers for the U.S. fleet.

REFERENCES

(Alekhin et al., 2013a) M. Alekhin, D. Biner, K Krämer, P. Dorenbos, (2013) J. Appl. Phys. 113 224904

(Alekhin et al., 2013b) M. Alekhin, J. de Haas, I. Khodyuk, K. Krämer, P. Menge, V. Ouspenski, P. Dorenbos, (2013) Appl. Phys. Lett. 102 161915

(Bearden, 1967) J. Bearden, (1967) Rev. Mod. Phys. 39, 78

(Beck et al., 2015) P. Beck, S. Payne, S. Hunter, L. Ahle, N. Cherepy, E. Swanberg, (2015) IEEE Trans. Nucl. Sci. 62, 3 1429

(Biermann et al., 2012) P. Biermann, V. de Souza, (2012) Astrophys. J. 746

(Birks, 1964) J. Birks, (1964) The Theory and Practice of Scintillation Counting, 1st Ed.

(Boatner et al., 2013) L. Boatner, J. Ramey, J. Kolopus, R. Hawrami, W. Higgins, E. van Loef, J. Glodo, K. Shah, E. Rowe, P. Bhattacharya, E. Tupitsyn, M. Groza, A. Burger, N. Cherepy, S. Payne, (2013) J. Cryst. Growth 379 63

(Brame, 2017) C. Brame, (2017) BOLD Fellows Program https://cft.vanderbilt.edu/programs/bold-fellows/

(Caudel, 2013) D. Caudel, (2013) AFM basic tutorial YouTube https://www.youtube.com/watch?v=dhfrZF3kAoQ

(Caudel et al., 2015) D. Caudel, S. Stewart, E. Grundstrom, (2015) AstroNavigation https://my.vanderbilt.edu/astronav/

(Caudel et al., 2016) D. D. Caudel, M. McCurdy, D. M. Fleetwood, R. A. Reed, R. A. Weller, B. Goodwin, E. Rowe, V. Buliga, M. Groza, K. Stassun, A. Burger, (2016) Nucl. Instr. and Meth. A 835 177

(Cherepy et al., 2008) N. J. Cherepy, G. Hull, A. Drobshoff, S. Payne, E. van Loef, C. Wilson, K. Shah, U. Roy, A. Burger, L. Boatner, W. Choong, W. Moses, (2008) Appl. Phys. Lett. 92 083508

(Cherepy et al., 2009a) N. Cherepy, B. Sturm, O. Drury, T. Hurst, S. Sheets, L. Ahle, C. Saw, M. Pearson, S. Payne, A. Burger, L. Boatner, J. Ramey, E. van Loef, J. Glodo, R. Hawrami, W. Higgins, K. Shah, W. Moses, (2009) Proc. SPIE 7449 74490F

(Cherepy et al., 2009b) N. Cherepy, S. Payne, S. Asztalos, G. Hull, J. Kuntz, T. Niedermayr, S. Pimputkar, J. Roberts, R. Sanner, T. Tillotson, E. van Loef, C. Wilson, K. Shah, U. Roy, R. Hawrami, A. Burger, L. Boatner, W. Choong, W.

Moses, (2009) IEEE Trans. Nucl. Sci. 56(3) 873

(Cho et al., 1999) J. Cho, C. Wang, H. Chan, J. Rickman, M. Harmer, (1999) Acta. Mater. 47 4197

(Cui et al., 2011) Y. Cui, R. Hawrami, E. Tupitysn, P. Bhattacharya, M. Groza, M. Bryant, V. Buliga, A. Burger, N. Cherepy, S. Payne, (2011) Solid State Commun. 151 541

(Dorenbos et al., 1995) P. Dorenbos, J. de Haas, C. van Eijk, (1995) IEEE Trans. Nucl. Sci. 42 2190

(Dorenbos, 2010) P. Dorenbos, (2010) IEEE Trans. Nucl. Sci. 57 1162

(Fleetwood et al., 1988) D. Fleetwood, P. Winokur, J. Schwank, (1988) IEEE Trans. Nucl. Sci. 35 1497

(Fleetwood et al., 1989) D. Fleetwood, P. Winokur, L. Riewe, (1989) IEEE Trans. Nucl. Sci. 36(6) 1963

(Fox, 2010) M. Fox, (2010) Optical Properties of Solids 2nd Ed. 250

(Grupen et al., 2011) C. Grupen, I. Buvat, (2011) Handbook of Particle Detection and Imaging

(Guiriec et al., 2010) S. Guiriec, M. Briggs, V. Connaugthon, E. Kara, F. Daigne, C. Kouveliotou, A. van der Horst, W. Paciesas, C. Meegan, P. Bhat, S. Foley, E. Bissaldi, M. Burgess, V. Chaplin, R. Diehl, G. Fishman, M. Gibby, M. Giles, A. Goldstein, J. Greiner, D. Gruber, A. von Kienlin, M. Kippen, S. McBreen, R. Preece, A. Rau, D. Tierney, C. Wilson-Hodge, (2010) Astrophys. J. 725 225

(Hoffman et al., 1991) G. Hoffman and A. Albrecht, (1991) J. Phys. Chem. 95 2231

(Hubbell et al., 2004) J. Hubbell, S. Seltzer (2004);

http://www.nist.gov/pml/data/xraycoef/

(Keman, 2006) W. Keman, (2006) IEEE Trans. Nucl. Sci. 53(1) 395

(Kerris et al., 1985) K. G. Kerris, S. Gorbics, (1985) IEEE Trans. Nucl. Sci. 32 4356

(Knoll, 2010) K. Knoll, (2010) Radiation Detection and Measurement 4th Ed.

(Kozma et al., 2003) P. Kozma, P. Kozma Jr., (2003) Nucl. Instr. and Meth. A 501 499

(Krause et al., 1979) M. Krause, J. Oliver, (1979) J. Phys. Chem. Ref. Data 8, 329

(Li et al., 1999) Y. Li, C. Wang, H. Chan, J. Rickman, M. Harmer, (1999) J. Am. Ceram. Soc. 82(6) 1497

(Medalia, 2010) J. Medalia, (2010) Detection of Nuclear Weapons and Materials: Science, Technologies, Observations, Congressional Research Service

(Moore, 1970) C. Moore, (1970) NBS Pub. NSRDS-NBS 34

Also avail. On Web, Table 1-2, http://xdb.lbl.gov/Section1/Table_1-2.pdf

(Moses et al., 2012) W. Moses, G. Bizarri, R. Williams, S. Payne, A. Vasil'ev, J. Singh, Q. Li, J. Grim, W. Choong, (2012) IEEE Trans. Nucl. Sci. 59 2038

(NASA, 2010a) NASA/Goddard Space Flight Center, (2010) http://svs.gsfc.nasa.gov/10688

(NASA, 2010b) NASA/Goddard Space Flight Center, (2010) https://web.archive.org/web/20121028154200/http://imagine.gsfc.nasa.gov/docs/science/know_l1/cosmic_rays.html

(Payne et al., 2009) S. Payne, N. Cherepy, G. Hull, J. Valentine, W. Moses, W. Choong, (2009) IEEE Trans. Nucl. Sci. 56 2506

(Payne et al., 2011) S. Payne, W. Moses, S. Sheets, L. Ahle, N. Cherepy, B. Sturm, S. Dazeley, G. Bizarri,, W. Choong, (2011) IEEE Trans. Nucl. Sci. 58 3392

(Payne et al., 2014) S. Payne, S. Hunter, L. Ahle, N. Cherepy, E. Swanberg, (2014) IEEE Trans. Nucl. Sci. 61 2771

(Ramachers et al., 2007) Y. Ramachers, D. Stewart, (2007) J. Instrum. 2 12003

(Perea et al., 2015) R. Perea, A. Parsons, M. Groza, D. Caudel, S. Nowicki, A. Burger, K. Stassun, T. Peterson, (2015) J. Astron. Telesc. Instrum. Syst. 1(1) 016002

(Reddy et al., 2016) F. Reddy, A. Morrow (2016); http://www.nasa.gov/feature/goddard/2016/nasa-celebrates-25-years-of-breakthrough-gamma-ray-science

(Su et al., 2010) M Su, T. Slatyer, D. Finkbeiner, (2010) Astrophys. J. 724 1044

(Unterweger et al., 2010) M. Unterweger, D. Hoppes, F. Schima, J. Coursey (2010); http://www.nist.gov/pml/data/halflife-html.cfm

(Vasil’ev et al., 2014) A. Vasil’ev, A. Gektin, (2014) IEEE Trans. Nucl. Sci. 61 235

(Winokur et al., 1986) P. S. Winokur, F. W. Sexton, J. R. Schwank, D. M. Fleetwood, P. V. Dressendorfer, T. F. Wrobel, D. C. Turpin, (1986) IEEE Trans. Nucl. Sci. 33 1343

(Yang et al., 2015) K. Yang, P. Menge, (2015) J. Appl. Phys. 118 213106

(Zhu, 1998) R. Zhu, (1998) Nucl. Instr. and Meth. A 413 297